WORLD RESOURCES INSTITUTE

TECHNICAL NOTE

AQUEDUCT FLOODS METHODOLOGY

PHILIP J. WARD, HESSEL C. WINSEMIUS, SAMANTHA KUZMA, MARC F.P. BIERKENS, ARNO BOUWMAN, HANS DE MOEL, ANDRÉS DÍAZ LOAIZA, DIRK EILANDER, JOHANNA ENGLHARDT, GILLES ERKENS, ESKEDAR TAFETE GEBREMEDHIN, CHARLES ICELAND, HENK KOOI, WILLEM LIGTVOET, SANNE MUIS, PAOLO SCUSSOLINI, EDWIN H. SUTANUDJAJA, RENS VAN BEEK, BAS VAN BEMMEL, JOLIEN VAN HUIJSTEE, FRANK VAN RIJN, BREGJE VAN WESENBEECK, DEEPAK VATVANI, MARTIN VERLAAN, TIMOTHY TIGGELOVEN, AND TIANYI LUO

ABSTRACT

Flooding is among the most serious and dangerous of all global risks, causing loss of life and damage to property, livelihoods, and economies. Flooding is also likely to intensify in the coming decades due to climate change. Additionally, economic growth and urbanization are putting more and more assets and people into flood-prone areas. Despite these dangers, flood risks are often underestimated and poorly managed due to the lack of data and actionable information, particularly in less-developed regions.

Aqueduct Floods is an online platform that measures riverine and coastal flood risks under both current baseline conditions and future projections in 2030, 2050, and 2080. In addition to providing hazard maps and assessing risks, Aqueduct Floods enables its users to conduct comprehensive cost-benefit analysis to evaluate the value of dike flood protection strategies.

Aqueduct Floods aims to empower disaster risk analysts and managers with quantitative information on flood risks and adaptation strategy costs, and to help inform policy and investment decision-making. This technical note explains in detail the framework, methodology, and data used in developing Aqueduct Floods to help users better interpret the risk information presented on the tool and understand the full strength and limitations of our data and methodology.

CONTENTS

Technical notes document the research or analytical methodology underpinning a publication, interactive application, or tool.

Suggested Citation: Ward, P.J., H.C. Winsemius, S. Kuzma, M.F.P. Bierkens, A. Bouwman, H. de Moel, A. Díaz Loaiza, et al. 2020. "Aqueduct Floods Methodology." Technical Note. Washington, D.C.: World Resources Institute. Available online at: www.wri.org/publication/aqueduct-floods-methodology.

1. BACKGROUND

Floods are widely recognized as one of the most costly natural hazards. The impacts of floods are projected to increase in many parts of the world (UNISDR 2015) due to climate change (Hallegatte et al. 2013; Hinkel et al. 2014; Vitousek et al. 2017; Ward et al. 2017; Winsemius et al. 2016; Woodruff et al. 2013), socioeconomic development in flood-prone areas (Jongman et al. 2012), and land subsidence (Syvitski et al. 2009; Brown and Nicholls 2015). Reducing the impacts of floods will require effective flood risk management, which, in turn, requires knowledge and understanding of current risk, future risk, and how that risk can be reduced through adaptation and risk management.

To answer this need, a consortium consisting of the World Resources Institute (WRI), Deltares, Vrije Universiteit Amsterdam's Institute for Environmental Studies (IVM), Utrecht University (UU), and the Netherlands Environmental Assessment Agency (PBL), with funding support from the Netherlands Ministry of Infrastructure and Water Management and the World Bank, have developed Aqueduct Floods, a global tool providing actionable information to analyze flood risks and understand the costs and benefits of interventions, such as dikes, to reduce flood risk.

Version 1 of the Aqueduct Global Flood Analyzer (online since 2014) allowed for analyses of river flood risk now and in the future, under the influence of climate change and socioeconomic change. The following components, identified as important by several stakeholders and missing from version 1, have been added to the new Aqueduct Floods:

- Coastal flood risk assessment, including future impacts of sea level rise, subsidence, and socioeconomic growth
- The ability to assess the costs and benefits of adapting to current and future flood risk
- Understanding of present-day flood protection standards
- Visualization of scenario and global climate model (GCM) uncertainty

This technical note explains in detail the framework, methodology, and data used in developing Aqueduct Floods. Section 2 gives an overview of the modeling framework and scenarios. Sections 3, 4, and 5 describe how hazard, exposure, and vulnerability were modeled individually. Section 6 explains how risk data were computed, and Section 7 describes how cost-benefit analyses are conducted. Section 8 discusses limitations.

2. OVERVIEW OF FRAMEWORK AND SCENARIOS

Flood Risk Model and Tool Framework

We simulated flood risk using a cascade of models within the Global Flood Risk with IMAGE Scenarios (GLOFRIS) modeling framework (Winsemius et al. 2013), and used GLOFRIS to assess the influence on river flood risk of natural climate variability (Ward et al. 2014) and future climate and socioeconomic change (Winsemius et al. 2016), as well as the costs and benefits of reducing river flood risk through dikes (Ward et al. 2017).

For Aqueduct Floods, several new aspects have been added to the GLOFRIS framework, and several major improvements have been made, including the ability to simulate coastal flood risk, projections of future subsidence, new projections of future population and gross domestic product (GDP), better representation of maximum potential damages and vulnerability, and an improved method for downscaling future climate impacts. In this section, we provide an overview of the GLOFRIS framework used in this tool.

Exposure and Vulnerability to Hazard: Affected Population, GDP, and Urban Damage

For this tool, risk is represented using three indicators: affected population, affected GDP, and urban damage. In brief, GLOFRIS simulates flood risk by combining information on hazard, exposure, and vulnerability. The data and methods used to represent hazard, exposure, and vulnerability, briefly described in this paragraph, are expanded upon in Sections 3, 4, and 5, respectively. The hazard is represented by inundation maps showing the flood extent and depth for floods of several return periods (2, 5, 10, 25, 50, 100, 250, 500, and 1,000 years) at a resolution of 5 × 5 arc minutes (5′ × 5′). This equates to

roughly 10 kilometer (km) × 10 km pixels at the equator. The hazard maps were regridded to 30 × 30 arc seconds (30″ × 30″)—about 1 km × 1 km at the equator.

Exposure is represented by different datasets, depending on the risk indicator. For affected population and affected GDP, exposure is represented by gridded maps of population count and GDP per cell, respectively; both of these datasets have a horizontal resolution of 30″ × 30″. For urban damage, exposure is represented using a land use map showing which cells are urban and which are nonurban (30″ × 30″). Urban cells, or built-up cells, are comprised of at least 50 percent human-made structures and are assigned a value of maximum economic damage per square kilometer (km^2) for each country. This represents the maximum damage (in US$ PPP [purchasing power parity] 2005[1] values per km^2) that could occur due to flooding in urban areas per km^2 per country.

Vulnerability is represented through depth-damage functions, which show the percentage of the maximum damage that would actually occur for different inundation depths; these depth-damage functions are only applied for the urban damage risk indicator.

Impacts per return period hazard level are computed as follows per grid cell: for urban damage, the percentage of damage relative to maximum damage is computed from the occurring water depth in that grid cell, and from the depth-damage relationship. For the other impact indicators, the amount of GDP or population in the grid cell is counted as impacted when water levels exceed 0 m. Each risk indicator is calculated for the return periods 2, 5, 10, 25, 50, 100, 250, 500, and 1,000 years, and expected annual impacts are then calculated as the area under the exceedance probability-impact curve (risk curve) (see, e.g., Meyer et al. 2009).

Climate Change Scenarios

In Aqueduct Floods, flood risk is calculated for 2010, 2030, 2050, and 2080. Future changes in climate and socioeconomic conditions are represented using three scenarios. Each scenario uses a combination of a representative concentration pathway (RCP) (van Vuuren et al. 2011) and a shared socioeconomic pathway (SSP) (van Vuuren et al. 2014) to represent future climate and changes in future socioeconomic conditions, respectively. The scenarios used are RCP4.5/SSP2, and RCP8.5/SSP2, and RCP8.5/SSP3.

Assessing Benefits of Flood Protection Dikes

Using Aqueduct Floods, it is also possible to assess the costs and benefits of reducing flood risk (in terms of urban expected annual damage [EAD]) by increasing the flood protection offered by dikes. This is achieved following the method developed in Ward et al. (2017), and described in Section 7. In brief, the benefits of increasing protection through dikes are defined as the difference between future EAD if dikes remain constant at assumed current height and future EAD if the height of dikes is increased. Costs are defined as the sum of investment and capitalized maintenance costs.

3. HAZARD MODELING

Aqueduct Floods now includes two hazard components, riverine and coastal floods. Both hazards are represented by global scale layers of inundation depth at 30″ × 30″ resolution, with different layers representing inundation depths for different annual average probabilities of occurrence. The hazard layers have been simulated without considering the presence of flood protection. Note that this does not mean that flood protection is not included in our risk computation. Instead of including it in the computations of riverine and coastal flood hazard, we include the effects of flood protection in the risk calculations by assuming zero damage below the assumed standard of protection (see Section 6).

River Hazard

To calculate the river hazard layers for the individual return periods, we used the GLOFRIS model (Ward et al. 2013; Winsemius et al. 2013). GLOFRIS applies a global hydrological model, PCRaster Global Water Balance (PCR-GLOBWB) (Sutanudjaja et al. 2018), with a river and floodplain routing scheme to make long-term simulations of discharges and flood levels for several climate conditions. The meteorological datasets of the European Union Water and Global Change (EUWATCH) program (Weedon et al. 2011) and the Inter-sectoral Impact Model Intercomparison Project (ISI-MIP) (Hempel et al. 2013) were used to force PCR-GLOBWB over various time periods, between 1950 and 2099. Based on PCR-GLOBWB output, we then applied extreme value statistics to derive the floodplain water volumes per grid cell for several flooding return periods (2, 5, 10, 25, 50, 100, 250, 500, and 1,000

years) for the current time (based on 1960–99 simulation) and future climate (2010–49, 2030–69, and 2060–99). These are then used as input to a volume spreading flood model (Winsemius et al. 2013) to convert the 5′ × 5′ flood volumes into maps of high-resolution inundation depth at a resolution of 30″ × 30″. We provide additional documentation on PCR-GLOBWB (version 2) and GLOFRIS model details, input data, and bias correction processes in Appendix A.1.1.

Flood Inundation Downscaling

We adapted the inundation downscaling algorithm described by Winsemius et al. (2013). The original downscaling approach performed downscaling per grid cell. Within our new downscaling approach, we follow the same principle but instead use a contributing basin approach, in which we downscale inundation volumes per river stretch. More details on our downscaling method and validation efforts can be found in Appendix A.1.2.

Coastal Hazard

To estimate coastal hazard, we used the Global Tide and Surge Reanalysis (GTSR) dataset (Muis et al. 2016) as a database of extreme water levels. GTSR is a global dataset of daily sea levels (due to tide and storm surge) for 1979–2014, based on the hydrodynamic Global Tide and Surge Model (GTSM). Surge is simulated using wind and pressure fields from the European Centre for Medium-Range Weather Forecasts (ECMWF) Re-analysis-Interim (ERA-Interim) dataset (Dee et al. 2011). Tide is simulated using a separate model, the Finite Element Solution 2012 (FES 2012) model (Carrère and Lyard 2003).

To establish extreme values for the required return periods, we fitted and applied a Gumbel distribution at all locations. Consequently, extreme tide and surge levels were established for 2, 5, 10, 25, 50, 100, 250, 500, and 1,000-year return periods. To translate near-shore tide and surge levels to overland inundation, we applied a geographic information system (GIS)-based inundation routine, similar to Vafeidis et al. (2018). We used gridded sea level changes from the Responses to Coastal Climate Change: Innovative Strategies for High-End Scenarios—Adaptation and Mitigation (RISES-AM) project (Jevrejeva et al. 2014) to simulate future extreme sea levels, and used subsidence estimates (see section below) to estimate how the terrain may change as a result of subsidence. See Appendix A.1.3 for more information on model enrichment and adjustments for coastal hazard modeling.

Subsidence Modeling

Land subsidence—the lowering of the land level—is an important variable used for calculating future flood risk. In many coastal areas, groundwater extraction is the dominant cause of human-induced land subsidence (Erkens et al. 2015; Galloway et al. 2016). Land subsidence was modeled on a global scale using three existing models—namely, the hydrological model PCR-GLOBWB integrated with the global Modular Finite-Difference Flow (MODFLOW) groundwater model (see de Graaf et al. 2017; and Sutanudjaja et al. 2018), and a land subsidence model (Erkens and Sutanudjaja 2015). More details on the subsidence modeling database and methodology can be found in Appendix A.1.4.

4. EXPOSURE

Baseline Exposure (2010)

In GLOFRIS, exposure is represented by different datasets, depending on the risk indicator being used. For urban damage, exposure is represented using a map showing the percentage of built-up areas per grid cell (30″ × 30″). Data for current built-up area per grid cell are taken from the History Database of the Global Environment (HYDE) (Klein Goldewijk et al. 2010). These data have a resolution of 5′ × 5′ and were therefore regridded to the 30″ × 30″ resolution. In the HYDE dataset, and therefore in this tool, this refers to all types of built-up areas and artificial surfaces such as pavement. For each of these cells, an estimate is made of the area that is residential, industrial, and commercial. A value of maximum economic damage per m^2 is estimated for residential, industrial, and commercial per country. For more information on the methods used to determine maximum economic damage for built-up areas, see Appendix A.2.2.

For affected population and affected GDP, exposure is represented by gridded maps of population count and GDP per cell, respectively; both have a horizontal resolution of 30″ × 30″. More details regarding the baseline maps for population and GDP can be found in Appendix A.2.1.

Future Exposure (2030, 2050, 2080)

Future built-up area percentages, which represent urban areas covered by at least 50 percent human-made structures, were taken from Winsemius et al. (2016). Data were computed using changes in gridded population and urban population from the Gladders Image-Slicing Multi-slit Option–Integrated Model to Assess the Global Environment (GISMO/IMAGE) (Bouwman et al. 2006), using the method described in Jongman et al. (2012).

The population and GDP maps are developed for future time periods (2030, 2050, 2080) using the shared socioeconomic pathways (SSPs). The SSPs have been developed by the research community to facilitate integrated assessments of climate impacts (van Vuuren et al. 2014). They provide possible pathways of society and related societal systems for the 21st century. Aqueduct Floods uses two of the five possible SSPs: SSP2 for optimistic and business-as-usual scenarios; and SSP3 for the pessimistic scenario. The data have been downscaled using the 2UP model. More details on future population and GDP exposure can be found in Appendix A.2.3.

5. VULNERABILITY

The damage estimation of the previous version of Aqueduct Floods (the Aqueduct Global Flood Analyzer) was conducted via a relatively limited vulnerability assessment that used a single stage-damage function for all urban areas. For the new version of Aqueduct Floods, vulnerability was assessed in more detail. Instead of looking at the overall urban damage, we estimated the flood damage to buildings over three occupancy types: residential, commercial, and industrial. For each of these occupancy types, total damage was calculated as the sum of structural and content damage. These were calculated using vulnerability curves per occupancy type.

These global flood depth-damage functions were taken from the database developed by Huizinga et al. (2017). They consist of normalized global damage curves up to six meters (m) (i.e., two stories), and maximum damage for structure and content per country. The maximum damage per country is based on GDP per capita and construction cost surveys (Huizinga et al. 2017; Appendix A.2.2).

The vulnerability of the population and GDP to floods was assessed as a binary condition: they are either affected or they are not. In any cell with inundation depths greater than 0, the population and GDP within that cell were considered 100 percent vulnerable (i.e., they are either affected or not, in a binary sense). We did not distinguish between different levels of vulnerability (forced migration, fatalities, etc.).

6. COMPUTATION OF RISK

Flood Protection

Flood protection measures, such as dikes, can reduce the impact of the flood hazard and therefore are important to consider when calculating flood risk. In Aqueduct Floods, default flood protection values are provided per administrative level 1 (e.g., states in the United States).[2] These values are based on the Flood Protection Standards (FLOPROS) model methodology (Scussolini et al. 2016). FLOPROS is a database of current protection standards for both riverine and coastal floods, developed specifically for Aqueduct Floods.[3] These modeled protection standards have been validated against actual flood protection standards in place in several regions (Scussolini et al. 2016). Since flood inundation is not simulated hydrodynamically, the framework does not account for the transfer of risk from better-protected upstream areas to downstream areas. See Appendix A.3 to read more about the validation process.

Existing flood protection levels must be updated for future years to reflect changing climatic conditions. For example, if flooding is projected to intensify, a 50-year flood protection level in 2010 may only protect against 25-year floods in 2050. To transform flood protection in future years, we used future loss-probability curves generated under a climate-change-only scenario (see below) and the baseline curves to find the future protection level. For example, if the current protection level for location A is 100 years, we calculate present-day losses associated with a single 100-year flood event using the baseline and find the probability of the same level of losses in the future using the climate-change-only future loss-probability curve.

Expected Annual Damage

Each impact indicator is calculated for the return periods of 2, 5, 10, 25, 50, 100, 250, 500, and 1,000 years for floods using the hazard (riverine and coastal), exposure (population, GDP, and urban assets), and vulnerability data. Impacts are translated into the expected annual damage (EAD)—or risk—using the exceedance probability-impact curve (Figure 1; see, e.g., Meyer et al. 2009). The curve is created by plotting the flood probabilities (i.e., 1/return periods) on the *x* axis and the impacts on the *y* axis. The area under the curve represents EAD; however, flood protection must be incorporated into the calculation before the integral of the area under the curve is taken. The flood protection is added to the risk curve as a vertical line.[4] All impacts to the right of the flood protection line (i.e., damage from smaller floods) are assumed to be protected against and are set to 0. EAD is calculated by integrating the area of the curve *to the left* of the flood protection line.

Figure 1 | **Risk Curve Used to Calculate Expected Annual Damage**

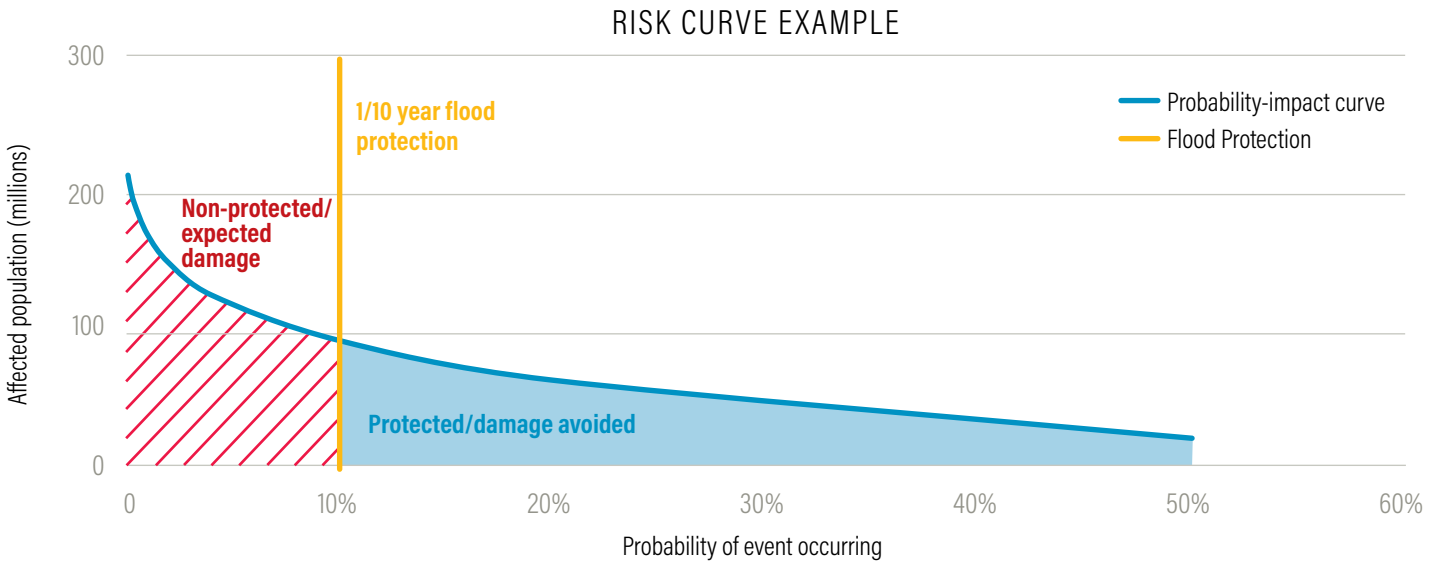

Source: WRI.

For riverine risk, EAD is calculated using five global circulation models. For coastal risk, EAD is calculated using the 5th, 50th, and 95th percentiles of spatially distributed sea level rise projections (Jevrejeva et al. 2014). The average, minimum, and maximum EAD are reported on Aqueduct Floods.

Drivers of Flood Impact in Future Years

Data on future impacts (flood risks) are split into four categories: total impact, impact from climate change only, impact from socioeconomic change (e.g., population and GDP growth, urban expansion) only, and (if coastal hazard) impact from subsidence change only. The last three items in this list—climate, socioeconomic conditions, and land subsidence—drive the change in future flood risks. However, only the total impact data account for compounding interactions among climate, socioeconomic, and subsidence factors. Therefore, impact from climate change only, socioeconomic only, and subsidence only must be scaled to match the change in total impact.

To do this, first the change from the total impact in future years to baseline impact is calculated:

$$C_{tot,2030} = I_{tot,2030} - I_{tot,2010}$$

where:

I = impact

C = change in impact from baseline

tot = total impact

Next, the change in impact from each of the drivers individually, compared to baseline impact, is calculated. Below we provide an example for change in impact, driven by climate change:

$$C_{cc,2030} = I_{cc,2030} - I_{tot,2010}$$

where:

I = impact

C = change in impact from baseline

tot = total impact

cc = climate change only

Finally, the drivers are turned into a ratio relative to one another and applied to the change in total impact:

$$D_{cc,2030} = \frac{C_{cc,2030}}{(C_{cc,2030} + C_{soc,2030} + C_{sub,2030})} \, x \, C_{tot,2030}$$

where:

D = driver

C = change in impact from baseline

tot = total impact

cc = climate change only

soc = socioeconomic only

sub = subsidence only

This process is repeated for estimated impact driven only by socioeconomic and subsidence changes, for the years 2030, 2050, and 2080 (nine ratios calculated in total). As with EAD, driver contributions are calculated for each global circulation model or sea level rise scenario and averaged at the end. Minimum and maximum climate contribution are also found and reported in Aqueduct Floods.

7. COSTS AND BENEFITS OF ADAPTATION

Using Aqueduct Floods, it is also possible to assess the costs and benefits of reducing flood risk by increasing the flood protection offered by dikes. This is just one form of adaptation to flooding and does not take into account other approaches, such as floodplain restoration and coastal mangroves, that also reduce flood hazard. The cost-benefit ratio is achieved following the method developed in Ward et al. (2017), from which the description below is taken or adapted. The methodology to derive coastal dike height and lengths is taken from van Wesenbeeck et al. (n.d.).

Analysis Time Frame

The cost-benefit analysis is carried out based on time periods defined by the user. First, the user defines the construction years[5] for the dike infrastructure. It is assumed that flood protection increases linearly during construction. Users must then choose the project start year and select the lifespan[6] of the infrastructure. Costs

and benefits will be calculated within this time frame: the analysis starts with the first year of construction and lasts until the lifespan is completed. As a default, the analysis starts in 2020, with the assumption that construction is complete by 2040. The analysis ends in 2100, 81 years after it began.

Estimation of Benefits

Within Aqueduct Floods, the user can define the current level of protection,[7] and the design protection level[8] (flood return period) against which dikes should protect in the future. The user must define in which year (2030, 2050, or 2080)[9] the design protection level should be valid. The benefits are then calculated as the difference between future EAD with the design protection and the EAD without additional protection. EAD without additional flood protection effectively means that existing dikes are maintained at their current height.

In order to get an annualized time series for the results, the EAD is first calculated for 2010, 2030, 2050, and 2080, as described above. EAD is then interpolated[10] for all years in the analysis time frame. Once this process is repeated for both the EAD with design protection and the EAD without additional protection, the benefits can be calculated. Benefits can begin accumulating as soon as construction starts, when construction is complete, or somewhere in between.[11] Any benefits achieved during construction are prorated based on the progress of the construction.

The benefits analysis is performed for each global circulation model and averaged at the end.

Estimation of Costs

Costs are calculated by summing annual investment and capitalized maintenance costs. Since EAD (and therefore benefits) is calculated in Aqueduct in US$ 2005 purchasing power parity (PPP), the estimates of unit investment costs per km of dike and m of dike heightening must also be in US$ 2005 PPP. The user can either enter a user-defined unit investment cost or use the default values (available per country).[12] See Appendix A.4.1 for more details on the default unit investment costs and Appendix A.4.2 for more details on estimating the dike infrastructure dimensions (km length per m height).

The total investment cost of the infrastructure (i.e., unit cost × dimensions) is annualized by first dividing it into equal intervals—where the number of intervals equals the number of construction years—and then turning the intervals into a cumulative sum. Once the annualized investment cost is calculated, the maintenance rate[13] is applied and added to the investment cost. The total maintenance expense in the last year of construction is used as the annual maintenance cost for all remaining years of the infrastructure.

The discount rate,[14] which can be customized, is applied at the end of the calculation. If not specified, the default rate is 5 percent. The discount rate is applied using the following equation:

$$final\ annual\ cost = \frac{(annual\ investment\ cost + annual\ maintenance\ cost)}{(1 + discount\ rate)^{year\ sequence}}$$

where:

year sequence = the number of years since construction began

8. LIMITATIONS

Uncertainties in future projections of both climate change and socioeconomic development need to be taken into account when interpreting analysis results generated by Aqueduct Floods. We provide a wide range of plausible scenarios and estimates using different climate models, aiming to give users, to some degree, the ability to evaluate and include uncertainties in their analyses.

Trade-offs between data availability and accuracy are one of the inherent limitations of global models. Efforts have been made to collect and develop new global datasets (e.g., existing flood protection, vegetation-corrected digital elevation model) for evaluating flood risks worldwide. However, assumptions are made when required data are not available at the global scale. It is also worth highlighting that simplification schemes (e.g., state-to-country aggregation, protection-level elevation) are adopted in the tool's on-the-fly-calculations to enhance computational performance.

Currently, only dikes are included as the intervention method in our flood protection cost-benefit analyzer. However, we understand that dikes might not be the (or the only) way to mitigate flood risks in many places. Other flood protection schemes, such as dams, mangroves, and early warning systems, should all be considered and evaluated when information is available and the situation applicable. We plan to further develop Aqueduct Floods to include more protection options, particularly green infrastructure, in future iterations of the cost-benefit analyzer.

While our tool measures both riverine and coastal flood risks, these hazards are evaluated separately, as the interaction, or the compound risks, between river and storm surges are not modeled in our analysis. On the one hand, simply adding damage estimates for riverine and coastal together could result in double-counting; on the other, some areas may suffer increased hazard due to compound effects. The tool also assumes that flood events are entirely independent of each other. This means that in the event a certain area experiences two floods very close in time, residual flooding impacts in the area not yet recovered from the first flood are not accounted for in our damage assessment.

The impact of floods on the economy and people's livelihoods could be a result of direct damages (e.g., flooded properties or infrastructure) as well as indirect ones (e.g., disrupted transportation or broken power lines). Indirect damages are not yet incorporated into our risk model. While our tool provides global coverage and comparability on flood risk data, when diving deep into specific locations, additional aspects of risks need to be considered and modeled to achieve a more comprehensive assessment.

APPENDIX

A. 1 Hazard Modeling

A.1.1 River hazard

The hydrological model, PCRaster Global Water Balance, version 2 (PCR-GLOBWB 2), simulates per time step the water volume that resides in the floodplains of rivers at a resolution of 5′ × 5′ (ca. 10 km × 10 km at the equator). Simulations are carried for (a) current climate conditions, using a reanalysis forcing dataset, and (b) future climate conditions, using data from several different global climate models (GCMs) forced with several representative concentration pathways (RCPs).

The input data used to carry out the hazard simulations for the current and future periods in this tool are described in detail in Winsemius et al. (2016). In brief, for current conditions, we used the European Union Water and Global Change (EUWATCH) forcing data (Weedon et al. 2011) over the period 1960–99, while for future conditions we used the Inter-sectoral Impact Model Intercomparison Project (ISI-MIP) forcing data (Hempel et al. 2013) for the periods 2030 (by running over the period 2010–49) and 2050 (by running over the period 2030–69), as well as 2080 (2060–99). Note that the exposure data for current conditions represent the situation in 2010 (not 1960–99). The main differences between the method described in Winsemius et al. (2016) and the method applied to develop the hazard layers used in Aqueduct Floods are (a) we have run the hydrological simulations with a newer version of PCR-GLOBWB, with a higher spatial resolution—that is, PCR-GLOBWB 2 at the spatial resolution of 5′ × 5′ (see Sutanudjaja et al. 2018 for new features and details); (b) we have applied an improved bias correction scheme; and (c) we have used a slightly modified downscaling scheme. Below, we briefly describe these modifications.

Winsemius et al. (2016) argue in their supplementary materials that a bias correction on the climate scenarios is required because the input climate datasets are only bias-corrected based on daily statistics. They thus may still contain bias in the autocorrelation of rainfall in time, at both short and long (yearly) time scales, as demonstrated by Johnson et al. (2011). Therefore, an additional bias correction was required. In Winsemius et al. (2016), this bias correction was applied by using a model-model difference in flood risk rather than by applying a bias correction within the hazard simulations themselves before performing the hazard map downscaling procedure. For Aqueduct Floods, we performed an additive correction method within the space of the extreme value distributions of the flood volumes. The extreme volumes obtained from the run forced with the observation-based EUWATCH dataset (1960–99) were assumed as the present-day values, and their changes in future flood volumes were calculated, for all GCMs, from differences between the values in future (RCP and GCM combination) and historical (GCM) conditions. The procedure to obtain corrected future volumes, "future corrected," is summarized in the following equation:

$$future\_corrected = present\_watch + (future\_gcm - present\_gcm)$$

with the *present_watch* representing present-day values based on the EUWATCH run, and *present_gcm* and *future_gcm* indicating values obtained from GCM runs in historical (under present-day greenhouse gas concentration forcing) and future (for various RCP scenarios) simulation periods.

The procedure is also illustrated for a given grid cell in Figure A1. For a future flood volume with bias for a given probability (indicated in Figure A1 using return periods)—estimated from a run with future conditions (RCP and GCM combination)—we calculated its change to the present-day value using the same GCM run under present-day greenhouse gas concentration forcing. We then imposed the difference to the present-day run forced with the EUWATCH dataset. For instance, let us assume that a run for RCP 4.5 using the Hadley Centre Global Environmental Model version 2—Earth System (HadGEM2-ES), a GCM, in 2050 produces a flood volume for the 10-year flood of 5 million cubic meters (m^3) for a given grid cell. Its flood volume in the GCM simulation under present-day climate is, for example, 2 million m^3. We then look up the flood volume of a 10-year event in the present-day in the EUWATCH run; for example, 4 million m^3. This means that the bias corrected flood volume for RCP 4.5 using HadGEM2-ES in 2050 is 4 million + (5 million – 2 million) = 7 million m^3. Note that in regions with simulated reduced extreme rainfall, the flood hazard may also go down, resulting in a negative bias correction. We always use a lower limit of 0 m^3.

Figure A1 | **Illustration of Bias Correction Procedure**

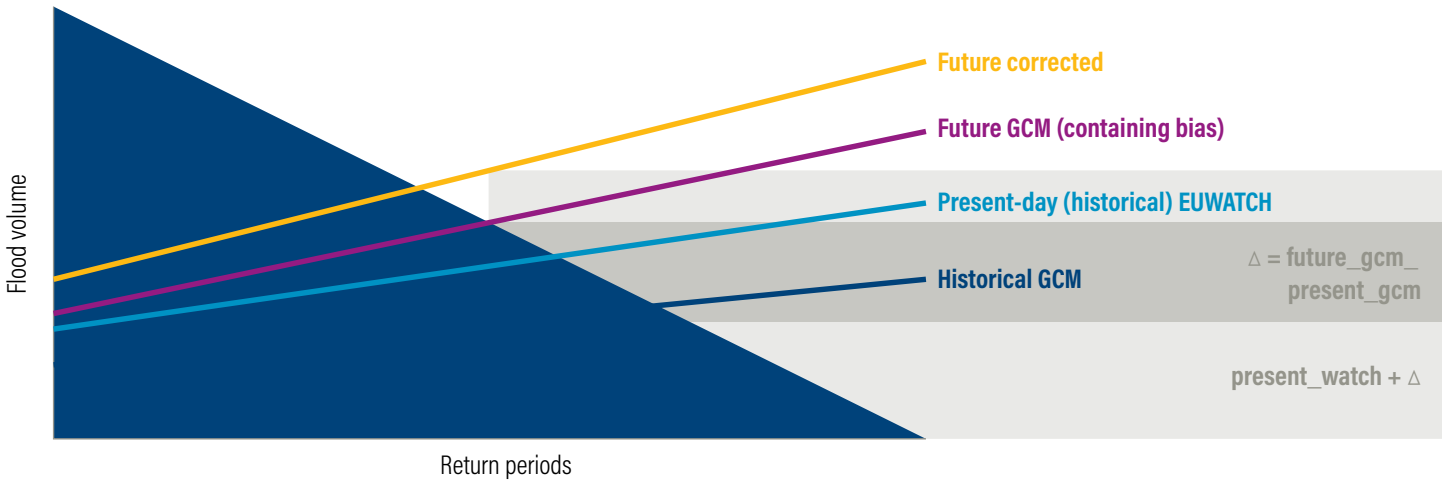

Source: Authors.

A.1.2 Flood inundation downscaling

We performed the following steps to downscale a given flood volume map to 30″ × 30″ resolution:

We used the 30″ × 30″ Hydrological Data and Maps Based on Shuttle Elevation Derivatives at Multiple Scales (HydroSHEDS) (Lehner et al. 2008) as our primary digital elevation model (DEM). To cover areas above 60th parallel north, we combined HydroSHEDS with the 30″ × 30″ Global 30-Arc-Second Elevation (GTOPO30) (Gesch et al. 1999) and 1 km HYDRO1k (Verdin and Greenlee 1996) datasets.

We derived Height-above-Nearest-Drain (HAND) (see Nobre et al. 2011 for further details) using the minimum Strahler threshold (in our case 6), up to the highest Strahler order found globally. The sensitivity of this assumption is discussed in Winsemius et al. (2013).

We masked out subbasins that contribute to the minimum Strahler threshold and accumulate the flood volumes per subbasin. We then used the HAND map belonging to the minimum Strahler order (in our case 6) to spread out the flood volume over the high resolution DEM. Using HAND instead of ordinary topography ensures that water is always spread out from the low-lying river cells to further upstream. This provided inundation for the rivers with the lowest Strahler order considered.

We repeated this procedure, but then taking out subbasins of one order higher, two orders higher, and so on, subsequently providing inundation for the higher-order subbasins.

The code to perform this inundation downscaling can also be applied to more granular hydrological model outputs and is contributed to the open-source hydrological modeling package *wflow* (Schellekens 2014). It can be found on https://github.com/openstreams/wflow. The flood routine can be found under https://github.com/openstreams/wflow/blob/master/wflow-py/Scripts/wflow_flood.py.

Similarly, as performed in Ward et al. (2017), we performed benchmarking of the derived global fluvial inundation hazard maps, particularly the ones derived from the EUWATCH run, using riverine hazard maps from more localized data sources. Figure A2 shows a spatial comparison between the global inundation extent maps and local inundation extent maps over some case studies. Based on Figure A2 and following the procedure outlined in Ward et al. (2017), we calculated three verification scores commonly used in flood forecasting verification. The first is the hit rate, *H*, which estimates the fraction of our derived global flooded area to coincide with the local flood map. *H* ranges from 0 (poorest score) to 1, which indicates that the global map captures all flooded areas suggested by local maps. As *H* does not penalize false flooded areas in the global map, we also calculated the false alarm rate, *F*, which ranges from 0 (best score), which means that no grids are incorrectly classified as inundated, to 1, which indicates that all inundated pixels are false. Lastly, we also estimated the critical success index, *C*, which is a combined score for *H* and *F* (see Ward et al. 2017 for details). Table A1 lists the verification scores for the case studies. The scores are comparable to those in the previous study by Ward et al. (2017).

Table A1 | **Inundation Verification Scores**

AREA	HIT RATE	FALSE ALARM RATE	CRITICAL SUCCESS INDEX
Bangladesh	0.55	0.31	0.49
Saxony (Germany)	0.84	0.52	0.44
Chao Phraya (Thailand)	0.60	0.31	0.47
Severn (UK)	0.81	0.68	0.30
Thames (UK)	0.59	0.51	0.37
St. Louis (USA)	0.88	0.27	0.67

A.1.3 Coastal hazard

The Global Tide and Surge Reanalysis dataset (GTSR) has been extensively validated, as described in (Muis et al. 2016, 2017). A recognized shortcoming of GTSR has been the poor representation of tropical cyclones. These storms are extremely intense and characterized by very sharp gradients in pressure and wind. These gradients are poorly represented in the European Centre for Medium-Range Weather Forecasts (ECMWF) Re-analysis-Interim (ERA-Interim) dataset. We therefore decided to enrich GTSR using a historical storm track archive to represent tropical cyclones. These tropical cyclones are simulated using the International Best Track Archive for Climate Stewardship (IBTrACS) archive, which provides a global dataset of historical best tracks. We used all tracks over the period 1979–2014, converted these into wind and pressure fields, and simulated water levels accordingly. We combined the time series of GTSR and the cyclone track simulations by using the highest value found within the time series and established extreme values using a Gumbel extreme value distribution fit on the annual extremes.

To translate near-shore tide and surge levels to overland inundation, we applied a GIS-based inundation routine, similar to the approach in Vafeidis et al. (2018). The routine inundates areas that are hydraulically connected to the sea at a given extreme sea level. The model uses the Multi-Error-Removed Improved-Terrain (MERIT) DEM (Yamazaki et al. 2017) at a 30″ × 30″ resolution as underlying topography.

We used gridded sea level changes from the Responses to Coastal Climate Change: Innovative Strategies for High-End Scenarios—Adaptation and Mitigation (RISES-AM) project (Jevrejeva et al. 2014) to simulate future extreme sea levels. These projections simulate a range of possible outcomes based on different sea level projection models. We chose the 50 percent projection for this project and have also established inundation estimates using the 5th and 95th percentiles. We included these projections by selecting for each extreme sea level the nearest pixel of the sea level rise grid and adding this additional water level to the extreme sea level.

Furthermore, we used subsidence estimates (see Section 3) to estimate how the terrain may change as a result of subsidence. We included subsidence, simulated at 5′ × 5′ by spatially interpolating these to the resolution of the MERIT terrain dataset and adding the subsidence estimates to the terrain, before processing the inundation.

MERIT is a reprocessed Shuttle Radar Topography Mission (SRTM) dataset that largely reduces noise factors as well as offsets due to vegetation. This is very important in coastal regions when simulating coastal flooding (Yamazaki et al. 2017). We accommodated three important factors in the inundation routine that are not regularly taken into account in global-scale coastal inundation modeling, but which can acutely impact inundation estimates:

We used a resistance factor to simulate the reduction of flooding as one moves inland. This resistance factor is important to consider as tides and storm surge events have a limited time span, and therefore their flood peak and associated volume can only penetrate inland to a certain degree. We applied this reduction factor over a Euclidean distance from the nearest coast line point. The resistance factor was set to 0.5 m/km based on visual validation for flood events in Brittany (France) and Texas (United States). In several other studies attenuation factors varying between 0.1 and 1.0 m/km were used (for a review, see Vafeidis et al. 2018), but no (land use–based) guidelines yet exist for applying this factor.

We multiplied the resistance factor by a weight proportional to the amount of water in each cell within the Euclidean pathway toward a land cell under consideration. In this way, grid cells that are marked as land within the terrain model, but in fact represent areas with large amounts of open water where tides and surge extremes can easily penetrate far inland, are correctly simulated as cells with low resistance. This happens, for instance, in the Brahmaputra Delta in Bangladesh, where the MERIT terrain data show terrain values over most of the estuary, but where these cells in reality represent very large open water connections to the ocean. We estimated fractions of open water using a 30-year monthly surface water mask dataset at 30 m resolution, derived from the Landsat archive (Pekel et al. 2016).

We applied a spatially varying offset between mean sea level according to the Finite Element Solution 2012 (FES 2012) model, and the datum used by the terrain model MERIT (Earth Gravitational Model 96 [EGM96]) to ensure that the zero datum of our terrain and our extreme sea levels from GTSR are the same.

A.1.4 Subsidence modeling

The main steps involved in the production of the global subsidence map(s) are depicted in Figure A2.

Groundwater model

Production started with a two-layer groundwater model for the terrestrial part of the world, excluding Greenland and Antarctica (de Graaf et al. 2017). This model combined the Modular Finite-Difference Flow (MODFLOW) groundwater code (Harbaugh et al. 2000) with the hydrological model PCR-GLOBWB, where the latter is used to estimate groundwater recharge and groundwater use (abstraction), which drives the groundwater flow. The model ran at a resolution of 5′ × 5′ (~10 km^2 at the equator) for the period 1958–2016. The output consisted of monthly values for hydraulic head for the two model layers. The complete model cascade is described by Sutanudjaja et al. (2018).

Figure A2 | **Main Steps Taken in the Modeling and Construction of the Global Subsidence Maps**

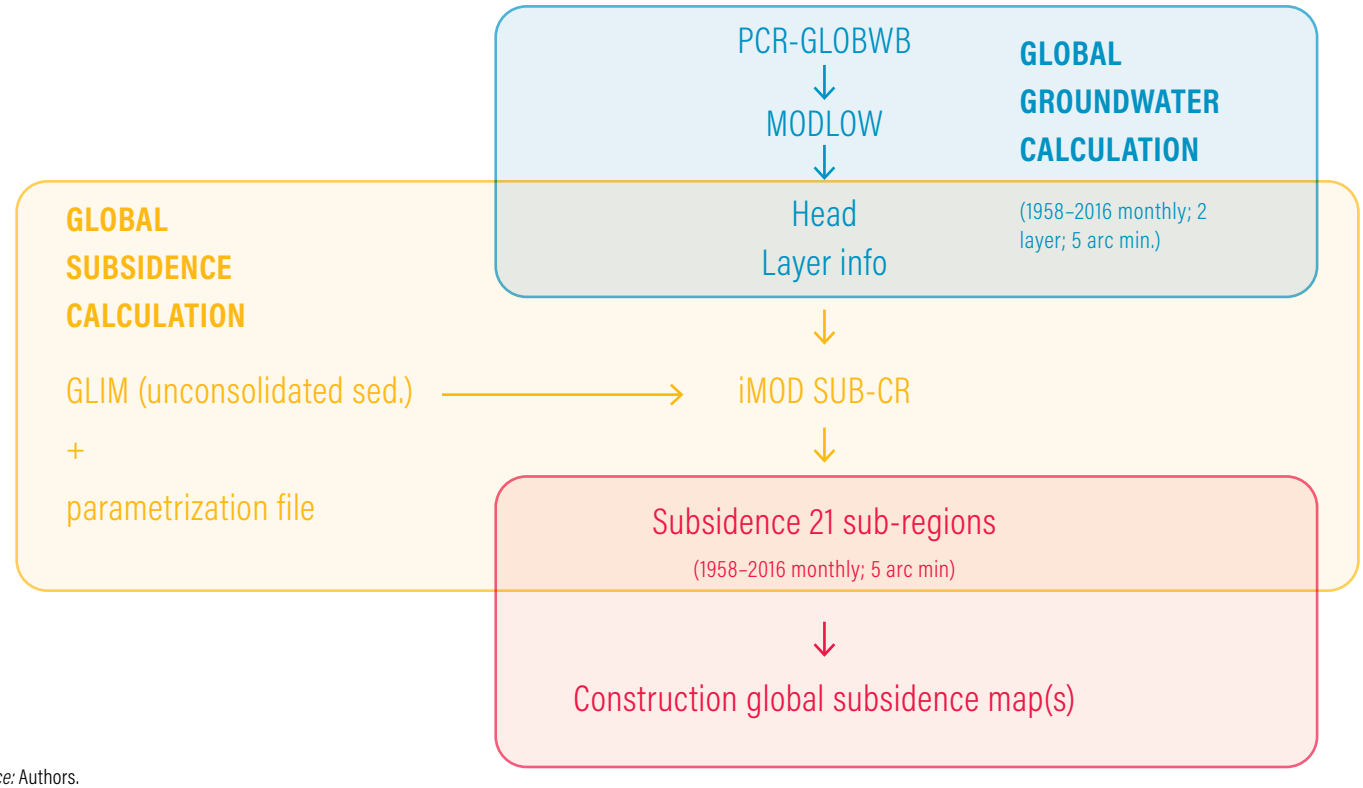

Source: Authors.

Subsidence model

Hydraulic head and top and bottom information of the two MODFLOW layers were used as inputs for the subsidence calculations. The calculations were carried out sequentially for each grid cell (1D vertical column) with the Deltares-developed MODFLOW package for land subsidence and aquifer system compaction (iMOD SUB-CR) code (Kooi et al. 2018). The SUB-CR subsidence package allows accounting for creep (often referred to as secondary compression that is independent of effective stress change). Subsidence is driven by head decline in the two main layers relative to the initial state in 1958. Elastic rebound or uplift is included upon head increase. Feedback of layer compression to flows and head is not included because MODFLOW model outputs are considered to already include such influences (without having been explicitly modeled). The two MODFLOW model layers were each subdiscretized into three layers in the compression calculations to improve the accuracy of calculated subsidence, while the head decline applied to each of the sublayers corresponds to that of the original MODFLOW layers.

Parameterization was based on an input file that specifies per original MODFLOW layer (a) three compression parameters, (b) preconsolidation state, and (c) interbed fraction. The global lithological map (GLiM), with global information on the distribution of unconsolidated sediments (Hartmann and Moosdorf 2012), was used to determine whether virgin compression and creep are employed, or solely elastic compression (for "consolidated" areas that can represent fractured and/or carbonate rock aquifers). The interbed fraction specifies the fraction of compressible sediments (clays/silts) within the model layer. A few other parameters, such as the specific weight of (un)saturated sediment, were fixed in the current approach.

A.2 Exposure Data

A.2.1 Baseline exposure

The present-day maps for Aqueduct Floods are based on 2010. For urban area, we used the data for 2010 from the History Database of the Global Environment (HYDE) (Klein Goldewijk et al. 2010). An initial set of global maps of population and gross domestic product (GDP) were also required for 2010. Over the years, global datasets of population and GDP have become increasingly available. However, at the time of development none of them appeared to be suitable for this particular project. Existing maps of global population distribution either lack the spatial specification of the urban and rural division or do not meet the requirement that the population input data be consistent with the reported numbers in the shared socioeconomic pathway (SSP) database.

Therefore, several freely available data sources were combined to model the baseline population distribution and GDP. To achieve this, first, a base grid was developed at 30″ × 30″. Country boundaries are primarily derived from the Global Administrative Areas dataset (GADM 2012). Several country boundaries were manually modified to match the UN country definitions as used by the International Institute for Applied Systems Analysis (IIASA) in the SSP database; Kosovo is included under Serbia; and South and North Sudan are joined into one country. In total 251 countries (International Organization for Standardization 3 [ISO3] areas) remained in this global information system (GIS) dataset. Of these, 57 countries were excluded in the modeling process as they could not be joined to the ISO3 codes of the SSP database. They are small countries like Andorra and Liechtenstein, islands (mainly overseas territories such as the Falkland Islands), and vast areas like Greenland and Antarctica. The country base grid includes the percentage of each cell that is land or water; this was achieved using a data layer showing land percentage per grid cell provided by Deltares (https://aqua-monitor.appspot.com/).

For baseline population, we started with the Oak Ridge National Laboratory (ORNL) LandScan 2010 population count map (Bright et al. 2011). As the total population per country in this map is different from the 2010 population stated in the SSP database, we used a correction factor per country to adjust the population per cell.

We then developed a baseline map of urban areas, based on data from the Global Human Settlement Layer (GHSL), developed by the Joint Research Centre (JRC) (http://ghsl.jrc.ec.europa.eu/). GHSL provides a map of built-up area at 1 km × 1 km resolution. We reclassified this map into a discrete map of urban and nonurban areas, using a threshold of 50 percent of built-up area to define urban land use. This threshold is based on visual comparison and correspondence with other high-resolution satellite data of built-up area.

Next we developed a map of baseline urban population. This is required in subsequent steps, as it allows us to better represent spatial differences in population between urban and nonurban areas. To do this, we overlaid the baseline map of urban areas with the baseline population map. Population within areas classed as urban is therefore defined as urban population in the following steps. Consequently, the absolute urban population numbers in the SSP database were not used directly.

For baseline GDP per capita per country, we used the GDP purchasing power parity (PPP) numbers and the population numbers from the SSP database

A.2.2 Estimation of maximum economic damage

To achieve a globally consistent approach, Aqueduct Floods uses the methodology of Huizinga et al. (2017) to estimate present-day maximum economic damage. Huizinga et al. (2017) found the following root function could be used to link GDP per capita to construction costs for each country:

$$y = ax^b$$

Where:

y = construction cost (2010 euros)

x = GDP/capita (2010 dollars)

a & b = constants (e.g., for residential buildings a = 24.08 and b = 0.385)

For this tool, we used the above equation to estimate construction costs per country in 2010, using the national level GDP per capita values from the SSP database. In order to transition from construction costs to maximum damage values, several further adjustments were necessary. We adjusted the construction cost values of the baseline and scenario following the suggested factors by Huizinga et al. (2017) for the different occupancy types. Such factors include depreciation, since the use of replacement values would overestimate the damage. Therefore, the construction costs are depreciated by a factor 0.6, the default used by Huizinga et al. (2017). Furthermore, Huizinga et al. (2017) suggest that buildings, particularly ones made of more resistant materials, be constructed of parts that will never be damaged. As all stage-damage curves for Aqueduct Floods are developed up to a 100 percent vulnerability fraction (see Section 3), we adjusted the construction costs for 40 percent of undamageable parts. In addition to these structural damage costs, the amount of content and inventory needed to be added to get the total potential maximum damage value. Reviewing the available literature for the different factors, Huizinga et al. (2017) suggest

that a global methodology take 50 percent, 100 percent, and 150 percent of the structural costs for residential, commercial, and industrial building content, respectively.

The above values refer to a country's average maximum damages per m^2 for individual objects, differentiated per occupancy type. The amount of residential, commercial, or industrial land use varies from country to country and within each country. As a proxy for the spatial distribution of different land classes between countries, we used Corine Land Cover data (EEA 2016) and compared for each European country the share of residential and commercial or industrial areas on the 100 m resolution dataset. For countries with these area types, the distribution between these two categories ranges between 75 percent and 95 percent for residential areas (86 percent average), and between 5 percent and 25 percent for commercial or industrial areas (14 percent average). Similar results can be found in a report by Buildings Performance Institute Europe (BPIE 2011) regarding floor space for various building types in Europe, where three-quarters of the building stock is residential, with nonresidential accounting for the remaining 25 percent. Since more detailed information is not yet available, both sources can only act as a rough proxy to estimate residential, commercial, and industrial areas in Aqueduct Floods' urban land use categories and are further restricted to Europe. Taking into account that every distribution we choose can only be an approximation for the global scale, the shares of residential, commercial, and industrial areas within the urban cells were set to 75 percent residential, 15 percent commercial, and 10 percent industrial, respectively. As for most large-scale models, Aqueduct Floods' impact model does not include information on building footprints but applies a land use–based approach for which we further estimated the density of buildings between 20 percent (residential) and 30 percent (commercial and industrial), again following the suggestions of Huizinga et al. (2017).

For future maximum damage values, we scaled the present-day values according to the change in GDP per capita per country between 2010 and each studied future time period.

A.2.3 Future exposure

To represent future urban area, we used the exposure maps developed by Jongman et al. (2015). To represent population and GDP, we developed a new method to represent the distribution between urban areas and nonurban regions. For this purpose, a different area map was required than the map of built-up area described previously. This was carried out using a new model; namely, 2UP (PBL 2018). In this model, urban and rural populations were distributed according to a map of urban area. This model included specific allocation procedures to explicitly account for urban population density change. 2UP is partly based on the same principles followed in the Land Use Scanner (Loonen et al. 2009) and uses the Geo Data and Model Server (GeoDMS) modeling framework. The resulting maps have a spatial resolution of 30″ × 30″. For Aqueduct Floods, the maps are developed for the present day (2010), and for future time periods (2030, 2050, 2080), using the shared socioeconomic pathways. The SSPs have been developed by the research community to facilitate integrated assessments of climate impacts (van Vuuren et al. 2014). They provide possible pathways for society and related societal systems in the 21st century. In total there are five SSPs; these are documented in the SSP database of IIASA, in which scenarios for population, urbanization, and GDP on global, regional, and national scales can also be found. The database contains data for 194 countries in 10-year intervals from 2010 to 2100. For this project, the population projections were used to extract total and urban population for the period 2010–80 in 10-year intervals, for SSP1, SSP2, and SSP3. Specifically, we used national population data based on the projection of IIASA's Wittgenstein Centre for Demography and Global Human Capital (IIASA 2013). In the same way, GDP PPP was extracted from the SSP database with the Organisation for Economic Co-operation and Development Env-Growth GDP projections. The projection data on urban share of the total population are developed by the National Center for Atmospheric Research (Jiang and O'Neill 2017). The growth rate of urban share per time step determines the growth of the urban population.

For a small number of countries in the SSP database, the population and GDP projections were available but not the urban share projections. In order to still be able to simulate urban growth for these countries, additional data were used to fill in these missing urban shares. For these countries the proportion of the total population that is considered urban in 2010—that is, the urban share—was derived from the Global Rural-Urban Mapping Project urban extent grid (Balk et al. 2006; CIESIN et al. 2011) in combination with LandScan gridded population count (Bright et al. 2013). The urban share is determined by superimposing the urban extent map on the gridded population map and extracting the proportion of urban population in each of these countries. For the future time steps (2020–80) the urban share for these countries was kept constant and assumed to be equal to the base year.

An overview of the overall approach can be found in Figure A3. Baseline maps of population, GDP, and urban areas were first developed. Then, for each country, 2UP was used to make projections of how these change in the future. Essentially, this involved three main steps. First, using data on growth in population, GDP, and urban density, the amount of additional urban area required per time step was estimated per country (country claims, see Appendix A.2.3.1). Second, the suitability of each grid cell for urban growth was calculated, based on physical and socioeconomic characteristics (suitability for urban growth, see Appendix A.2.3.2). Third, an allocation module was used to combine the country claims data and the suitability maps, resulting in projected urban growth (allocation module, see Appendix A.2.3.3). Finally, urban population was assigned to the urban cells with the same suitability maps. The modeling steps were repeated for each 10-year time interval. The model processes are explained in more detail in the following subsection.

Figure A3 | **Conceptual Framework of 2UP Model: Input, Processing, and Outcomes**

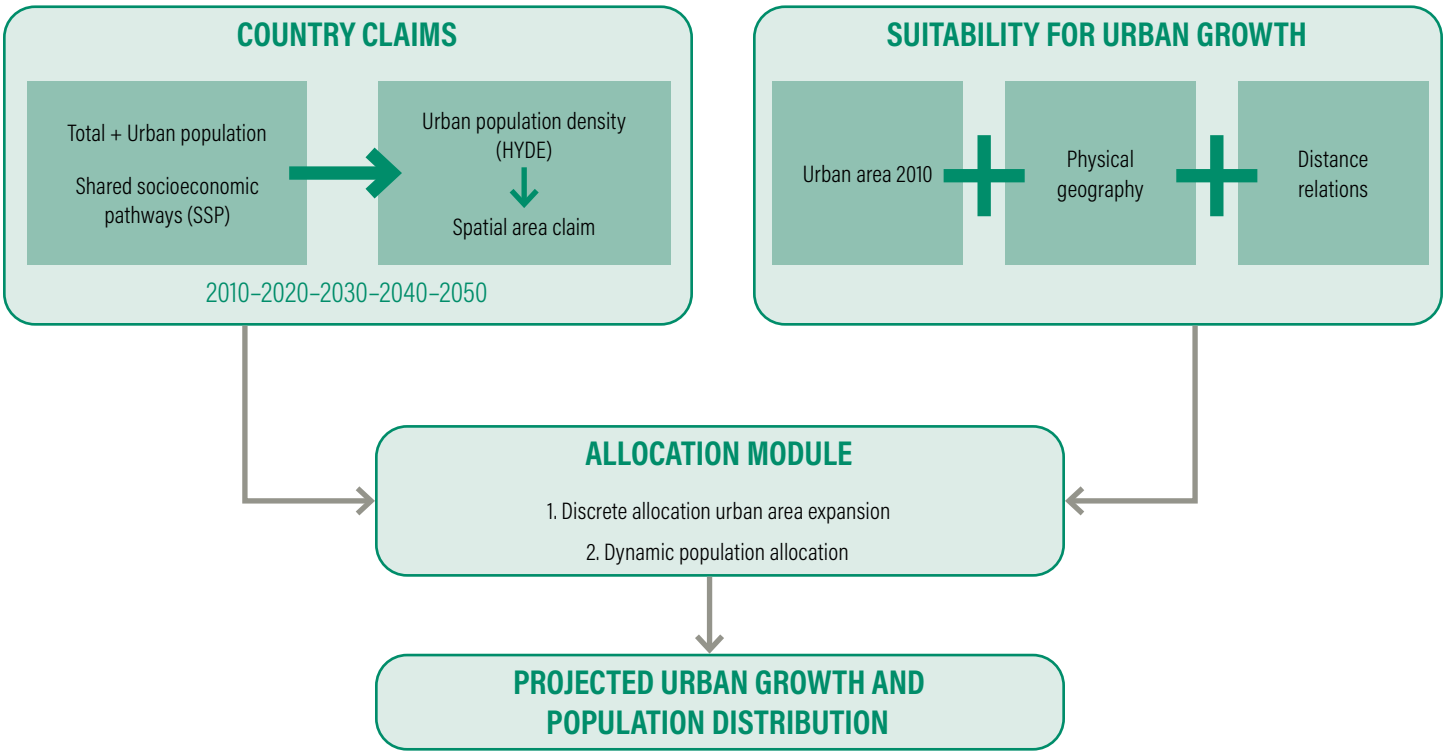

Source: Based on Figure 1 in PBL (2018).

A.2.3.1 COUNTRY CLAIMS

The next step was to estimate the change in (urban) population and GDP per country. The SSP database does not contain data on future urban area growth or a similar indicator like urban population density. To derive the urban area per country per time step, the corresponding national urban population (from the SSP database) in a time step was divided by the mean urban population density (from the HYDE database) in the former time step. A slight correction in the form of an index was made by using the HYDE 3.2 dataset. This dataset contains estimates of urban population density per country from 10,000 BC to 2100 AD (Klein Goldewijk et al. 2017, 2010) and is available for all SSPs. To develop the indices for each SSP scenario and country, the time series with absolute numbers of mean urban population density from HYDE were converted into an index series with base 2010 being equal to 1. In this manner, if mean urban population density was projected to decline, the urban area claim increases. In this way urban sprawl can be simulated by the model.

Change in population per country was derived directly from the SSP database (IIASA 2013). To estimate future change in urban population per country between time periods, in order to enable a comparison between countries, we used the relative growth rates derived from the urban population shares in the SSP database. This means that only the SSP country totals were retained but not the imposed urban-rural population division. Aggregated absolute urban population in the future gridded projections could therefore deviate from the absolute reported numbers based on the urban shares in the SSP database.

A.2.3.2 SUITABILITY FOR URBAN GROWTH

Spatial analyses to construct suitability maps

The spatial allocation of population distribution to the grid level was based on local suitability for urban land use and population growth. Suitability here can be considered as a proxy for the attractiveness of a location to stimulate or repel urban growth, based on a set of physical and socioeconomic characteristics. The suitability can be determined by quantifying the relation between the covariates and urban land use. This was done using an inductive approach; the suitability was determined empirically with the aid of a spatial analysis using historical data of urban land use.

The Atlas of Urban Expansion of the Lincoln Institute of Land Policy provides maps that represent urban land cover change between circa 1990 and circa 2000 for a sample of 120 cities across the globe with more than 100,000 inhabitants and distributed over nine world regions (Angel et al. 2012). The urban land use for each city was derived from Landsat images for the two time periods with a spatial resolution of 30 m × 30 m (Angel et al. 2005).

For the spatial analysis, the set of explanatory variables was superimposed on the urban land use for each of the 120 cities, and their values were extracted. Urban area for both time periods was taken into consideration, except for the analysis with distance to built-up area. Here, only the urban area that was built between the two time periods was used; urban area around 1990 was used as urban contour to determine the distance between newly built and existing urban area.

In the next step, histograms were plotted for each explanatory variable. In this way the relations between urban area and the variables were made visible. They all showed an inverse relation, which implies that with higher values of terrain roughness, travel time, distance to urban area and coast, the probability for new urban area decreases. The relations that were found were translated into probability frequency distributions, which were used in the 2UP model to transform the explanatory maps into suitability maps.

When simulating land use forward in time, there is inherently no other way than to assume constant relations between the geographical covariates and the future urban growth. Therefore, the distribution of future urban expansion and population is based on the relations that were found in the historical spatial analysis.

Although elevation and slope are both often referred to and used as explanatory variables for spatial patterns of urban growth, with grid cells covering approximately 1 km × 1 km, these variables might not be as indicative. Flat terrain at high elevations may be just as suitable for built-up urban area as flat terrain at low elevations. Additionally, the average slope of an area aggregated to 1 km × 1 km is rather coarse for explaining suitability for urban growth. Terrain heterogeneity, which describes a combination of heights and multidirectional slopes within an area, could contain more information on the suitability for urban growth. Therefore, the Terrain Roughness Index (TRI), which quantifies terrain heterogeneity, was used as covariate in the suitability mapping. TRI is calculated according to the method described by Riley et al. (1999), using a high-resolution DEM. For this purpose, a composite of SRTM v3 (Jarvis et al. 2006) and GTOPO30 (USGS 1996) elevation data was used. The SRTM v3 elevation map covers the globe between –60 and 60 degrees latitude, and is available with a spatial resolution of 1″ × 1″ (approximately 30 m × 30 m at the equator). The GTOPO30 (30″ × 30″) map was used to complete the elevation map for +/– 60–90 degrees latitude. The resulting TRI map was processed at 30 m × 30 m resolution, and each grid cell contains a discrete index value for terrain roughness. To be implemented into the model this map needed to be aggregated to 30″ × 30″. To avoid loss of detail as much as possible, for each TRI class (1–7) a map was compiled by counting the presence of that index value in the coarser grid cell. The seven maps in total were read into the model.

Travel time to the nearest city center is also considered an explanatory variable of urban growth and population distribution. A map with travel time (in minutes) to the nearest urban center was derived from a distance analysis based on road density and settlement data. The Global Roads Inventory Project (GRIP) dataset v1 (PBL 2009) was used, which contains a global road network. Populated places with more than 50,000 inhabitants were used as a settlement map.

Distance to urban area and distance to coast were also included in the 2UP model as covariates of urban growth. Both are based on the presence of surrounding urban land use, the latter also in combination with the proximity of the coastline. Urban area is modeled in 2UP, and therefore these two variables are not static but dynamically simulated over time. For the historical analysis, both distance variables were calculated for the baseline urban land use map (2010).

Suitability maps

In general, the earth's land surface is not considered completely habitable for human settlement. For this reason a land mask is constructed from multiple spatial data layers to exclude unsuitable grid cells for habitation. This mask was processed by overlaying the following data layers: surface water and permanent snow and ice cover. The Water Bodies Map dataset from the European Space Agency's Land Cover Climate Change Initiative (Defourny 2016) was used to mask global surface water. Permanent snow and ice cover was extracted from the Moderate Resolution Imaging Spectroradiometer (MODIS) Collection 4 global land cover dataset (Friedl et al. 2002), and these areas were excluded as allocable land.

Suitability represents the relative attractiveness of each grid cell for urban land use and population. The urban driver maps and the tables with the historically derived probability values were loaded into the model. To transform them into suitability maps, the variable maps were given the corresponding probability values.

The seven maps with TRI, one for each TRI class, containing the frequency of the index values per 30″ × 30″ grid cell, were combined into one suitability map. This was done by multiplying the probability and the frequency values for each TRI class and adding them together in one map.

The variables distance to urban area and distance to coast were calculated using the modeling software. Distance to urban area is an indicator based on the presence of urban land use at a location and its surroundings. It was calculated by taking the sum of the total amount of urban area in the neighboring grid cells after applying a relative weight based on their distance to the central grid cell. The weight quickly decreases with increasing distance. The number of neighboring cells that can contribute to this potential of each cell was restrained by applying a buffer of 10 km. Distance to coast was similarly calculated as distance to urban area and used as an indicator of urban potential. However, it was based on a combination of urban area and its distance to the coastline. The potential of urban area within 20 km of the coast was considered higher than that of urban areas outside this range. So the weight of potential of urban area decreases with distance to the coast.

The relative contribution of the individual suitability maps determined the total suitability at each location, which was eventually used in the allocation process. Ideally, the weights are determined by calibration of the model. However, at the time of modeling the resulting urban land use maps and population distribution, the results of the calibration procedure were not yet available. A new version of the 2UP model will include the calibration coefficients to weigh suitability maps.

A.2.3.3 ALLOCATION MODULE

Allocating urban expansion

The allocation of urban area within a country was based on the projected urban area claim, which was derived from the urban population claim, mean urban density in 2010, and the HYDE index. For each future time step, the projected amount of urban area (claim) was determined and the final suitability map was calculated. Thereafter, the urban area was allocated proportionally to the suitability map. This allocation procedure includes two steps: (1) the suitability within a country was sorted in a descending order, and (2) the urban area was allocated to the grid cells containing the highest suitability until the total claim was met. Both suitability and urban area were discrete across all cells of 30″ × 30″, and as such, each cell was defined as either urban or rural.

Allocating population

The allocation of population was based on the projected population change and suitability. The latter was assumed to be equal for the allocation of urban area and population. The model was directed at downscaling urban population and builds on the simulated urban land use map from the previous step. The downscaling was done recursively, which means the urban population distribution in time step *n* was used for the simulation of the time step *n* + 1. Thereby, for each time step the projected change in urban population was allocated within the urban area, proportionally according to the relative distribution of suitability in the urban area. The grid cells with the highest suitability received a proportionally larger share of the urban population change. Here also the allocation was weighted to the area of available land in a grid cell.

The remaining rural population was downscaled to the grid level in a straightforward way. The projected national-level rural population was disaggregated proportionally to the population distribution of LandScan (Bright et al. 2011). The population count in the latter was first transformed into fractions of the total population, which then served as a distribution surface to allocate the rural population. Rural population was only allocated to nonurban areas.

Allocating different scenarios

The spatial distribution of urban expansion and population growth that was simulated by the model was mainly driven by (1) national level population; (2) national level share in urban population, which represents urbanization; (3) national level urban density change; and (4) suitability mapping. The first three factors were SSP-specific, and their differences are exhibited in the model outcomes. The fourth factor, suitability mapping, was grid-level specific and primarily impacted the spatial patterns within a country. But it was static across the SSP scenarios. To implement variation based on the SSP storylines between the SSPs regarding suitability, two additional geospatial data layers were added to the suitability mapping: protected land and flood-prone area. For the protected land map the World Database on Protected Areas (WDPA) was used (IUCN and UNEP-WCMC 2009). The flood-prone area map represents river flood extent (1,000-year return period) and was collected from the Global Flood Risk with IMAGE Scenarios (GLOFRIS) framework (Ward et al. 2013; Winsemius et al. 2013). These two factors were selected as they can be used in a policy-related context; their influence on local suitability for urban growth can be linked to the SSP narratives. From these narratives an SSP-specific parameter value was deduced to modify local suitability and to account for local differentiation between scenarios. The final suitability was then determined by multiplying the parameter value with the local suitability value in cases of protected land, flood prone area, or both. Thus, for example, when a grid cell is located within protected land the suitability is set to zero for SSP1 and urban growth is excluded from this area. In Table A2, the parameter values are presented for each combination of SSP and suitability factor.

Table A2 | **SSP Specific Parameter Values for Suitability**

SUITABILITY FACTOR	SSP1	SSP2	SSP3
Protected land	0	0.5	1
Flood prone area	0	0.5	1

Source: PBL Netherlands Environmental Assessment Agency.

Disaggregation of GDP projections

Most datasets on economic development are still available mainly at the national level. For spatial analysis the national figures are often disaggregated to the grid level according to population density across a country. Only recently have such data become available on a subnational scale, which makes it possible to achieve higher precision than on a country scale. Gennaioli et al. (2013) developed a subnational dataset (tabulated) that includes GDP per capita in constant 2005 international US$. The database consists of 1,569 subnational regions (i.e., provinces, states, etc., depending on the country) across 110 countries. Although subnational GDP data are missing for most of the African continent, the data cover 74 percent of the world's land surface and 96 percent of its GDP. The temporal coverage is also country-specific and ranges from 1960 to 2010. Disaggregation of the national GDP projections to the grid level was based on the subnational data from this dataset whenever possible, in combination with national data from the SSP database. In this way the spatial variation in economic development within countries was taken into account, with the goal of developing an enhanced global gridded dataset of GDP.

The table with GDP per capita data was spatially joined with the country base grid, based on GADM country boundaries. The latter also include first-level administrative subnational boundaries. The regional GDP data could therefore be linked to the base grid. The division of subnational regions in the original database did not perfectly match the regional division in the GADM base grid. Therefore, several manual adjustments were necessary to correct for deviations. In this process, lower-level subdivision of regions in the original data needed to be aggregated to one region in the base grid in some cases. Consequently, the number of subnational regions in the end result was lower, but the coverage remained the same. When available, the reported regional value for GDP per capita for 2010 was used, followed by the most recent year. In case of missing data, national GDP per capita (SSP database) was used.

A.3 Validating FLOPROS

Flood Protection Standards (FLOPROS) is a database of current standards developed specifically for Aqueduct Floods (Scussolini et al. 2016). An extensive literature review was carried out, and supplemented with expert interviews, to derive a dataset of flood protection standards around the world. Since such information is not available for many regions, a modeling approach was also developed, as described in Scussolini et al. (2016). The original FLOPROS model values were calculated using the hazard and risk maps of GLOFRIS v1 as input. Since we now have new hazard and risk maps, the model was rerun with these to derive the state-level estimates that are used in the new version of Aqueduct Floods. Following the approach of Scussolini et al. (2016), we compared the modeled values with reported flood protection standards for several locations around the world (Figure A4). Such a comparison is difficult, since there is a disconnect between the state-level estimates of the FLOPROS model (which represent an average modeled protection standard per state) and the reported values, which are sometimes for an entire country, sometimes for a state, sometimes for a river basin, and sometimes for a city. However, they allow us to investigate whether the FLOPROS-modeled values are on the same order of magnitude as the reported values.

Values are shown for several locations for which reliable reported estimates of protection standards are available. These reported values are either shown as a range (minimum and maximum reported values) or a single value. FLOPROS model values are shown using the original data from Scussolini et al. (2016) and the FLOPROS model values using the data from the new version of Aqueduct Floods.

For most locations where the reported values provide a range, the FLOPROS model values are within or close to this range. An exception is Mozambique, where modeled protection standards are clearly lower than reported. Figure A5 also compares the flood protection standards from the FLOPROS model using the original data of Scussolini et al. (2016) and using the new simulations based on the new GLOFRIS data. For most locations, the values are similar.

The same method was applied to also estimate coastal flood protection standards at the state level, and a similar validation carried out (Figure A5). Overall, the model performs very well. The only location for which the reported values provide a range, and for which the FLOPROS model lies outside this range, is Durban, South Africa. However, note that reported values are for the city of Durban, while the FLOPROS model value is for the state in which it is located. Unsurprisingly, the value for the state is lower.

A.4 Underlying Cost Data

A.4.1 Estimating dike costs per country

First, we estimated unit investment costs of dikes in the United States at $7.0 million km/m (kilometer length × meter heightening). This estimate is based on reported costs in New Orleans (Bos 2008). It pertains to all investment costs, including groundwork, construction, and engineering costs, property or land acquisition, environmental compensation, and project management. We selected this value since it also is in the middle of other recent estimates for the United States and the Netherlands (Aerts et al. 2013; Jonkman et al. 2013). Moreover, it is close to the average cost of heightening reported in De Grave and Baarse (2011) of $6.6 million km/m heightening for 21 dike rings in the Netherlands; $6.7 million km/m heightening for 36 dike reaches in Canada (Lenk et al. 2017);

Figure A4 | **Validation of Modeled River Flood Protection Standards Using the FLOPROS Modeling Approach**

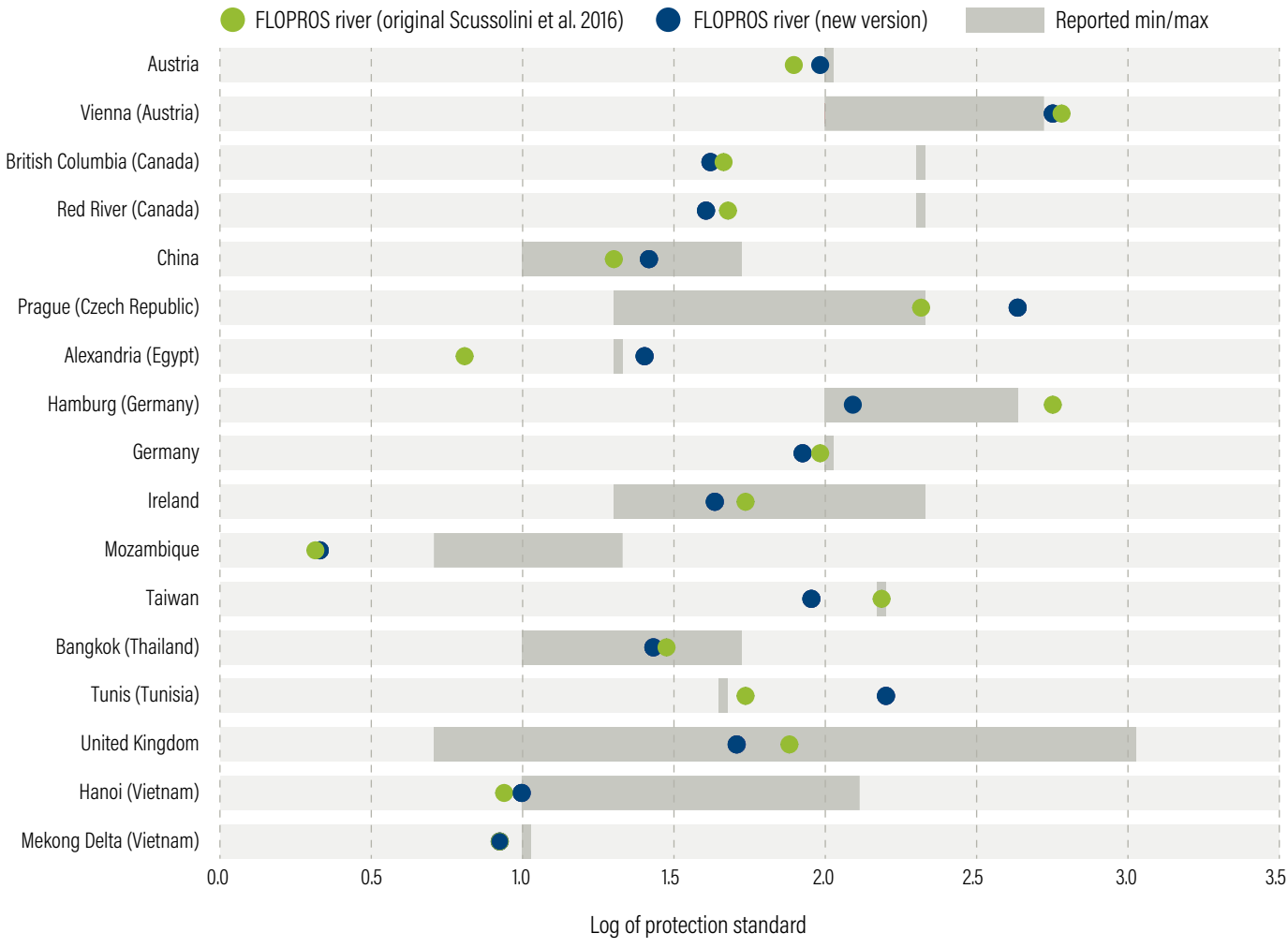

Source: Authors, based on Scussolini et al. 2016.

and $8.4 million km/m heightening for coastal dikes in the Netherlands (Lenk et al. 2017). Lenk et al. (2017) find that investment costs per meter heightening are well described by a linear function without intercept. They conclude that for large-scale studies it is sufficient to assume linear costs for each meter of heightening, including the initial costs. These cost estimates were then adjusted for all other countries by applying construction index multipliers (Compass International Consultants 2009) (based on civil engineering construction costs) to account for differences in construction costs across countries (Ward et al. 2010). These costs are all then converted to US$ 2005 PPP using GDP deflators from the World Bank and annual average market exchange rates between euros and dollars taken from the European Central Bank. Maintenance costs are represented as a percentage of investment costs per year, using either a default value of 1 percent per year or a user-defined value.

A.4.2 Estimating dike dimensions

For river flooding, we estimated the km length of dikes required by combining the river network map and the map of urban areas used in GLOFRIS (both 30″ x 30″). We calculated the length of rivers of Strahler order 6 or higher (since these are the rivers for which inundation is simulated in GLOFRIS) flowing through urban areas. To calculate the (increase in) dike height needed for each future scenario to facilitate protection against floods for various magnitudes and

Figure A5 | **Validation of Modeled Coastal Flood Protection Standards Using the FLOPROS Modeling Approach**

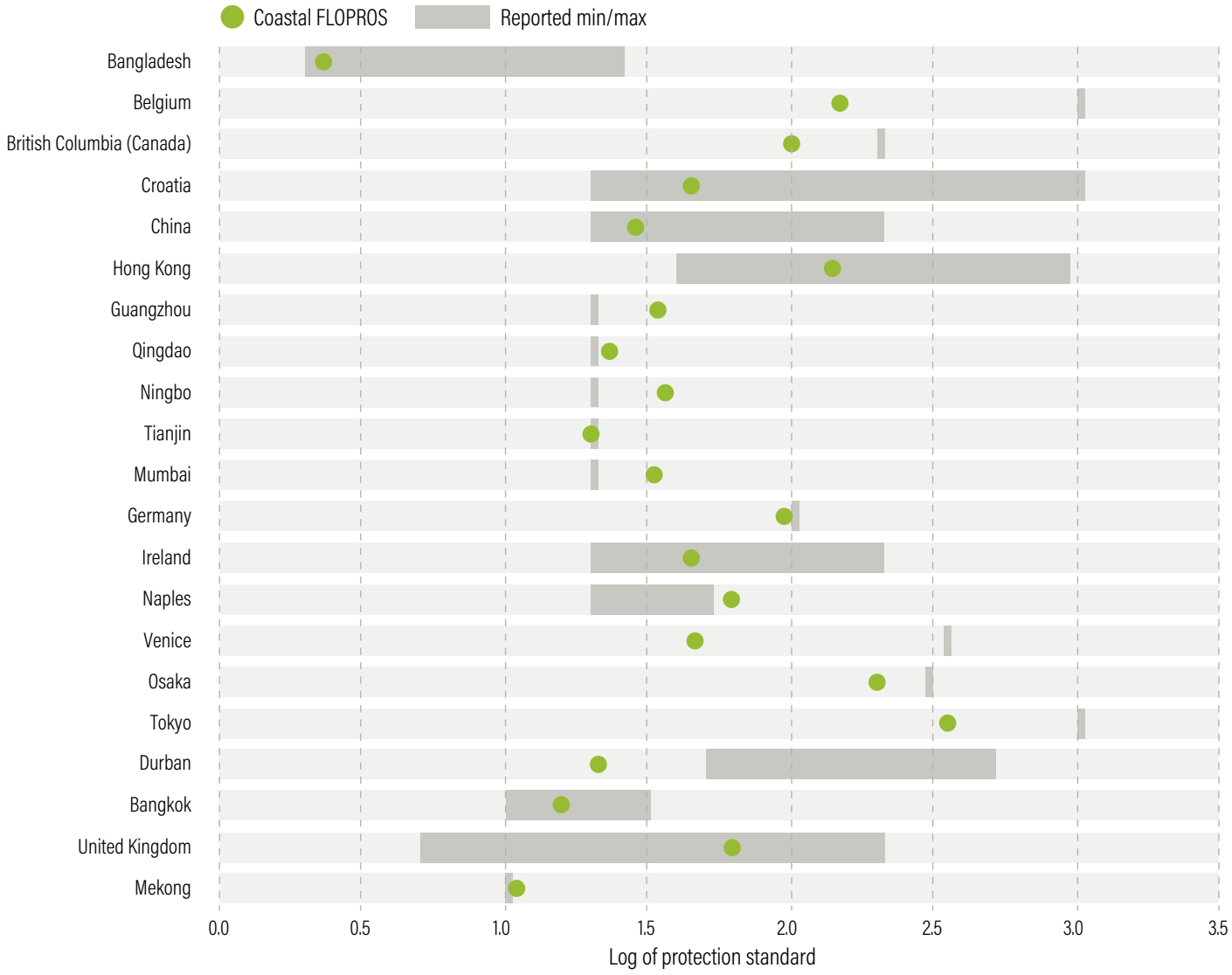

Note: Values are shown for several locations for which reliable reported estimates of protection standards are available. These reported values are either shown as a range (minimum and maximum reported values) or a single value. FLOPROS model values using the data from the new version of Aqueduct Floods.
Source: Authors, based on Scussolini et al. 2016.

associated return periods, for each river cell we estimated the required height of the dike for a given return period of protection by converting the discharge occurring with the return period into a flow depth. For a given scenario and protection level, and for a given grid cell, we established the heights of the dikes as follows. First, we retrieved the discharge occurring with the return period associated with the required protection level from a Gumbel distribution of discharges, established from GLOFRIS (Ward et al. 2013). Dikes are usually not built directly on the banks of the river but at a certain distance from the banks within the floodplain. We have here assumed that they are built at a distance of one times the channel width from the river banks. The width and bankfull depth of the channel are taken from the hydrological model PCR-GLOBWB (part of GLOFRIS framework), using

$$Q = hB\frac{1}{n}R^{2/3}\sqrt{i} \quad \text{(Eq. 1)}$$

where Q is the discharge [$L^3 T^{-1}$], h is the flow depth [L], B is the flow width [L], n is the Manning roughness [$T L^{-1/3}$], R is the hydraulic radius [L] (equal to $hB/(2h + B)$), and i is the slope of the channel [-]. In large rivers, flow depth is much smaller than flow width, and R can be approximated by h, reducing Eq. 1 to

$$Q = B\frac{1}{n}h^{5/3}\sqrt{i} \quad \text{(Eq. 2)}$$

In our case, a part of the flow is through the main channel and over the part of the floodplain that lies between the dikes, both having different dimensions and roughness values. We therefore split Eq. 2 into a channel part and a floodplain part as follows:

$$Q = \left[B_c\frac{1}{n_c}h^{5/3} + B_f\frac{1}{n_f}(h - h_{bf})^{5/3}\right]\sqrt{i} \quad \text{(Eq. 3)}$$

where c and f are channel and floodplain, respectively, and h_{bf} is the bankfull channel depth [L]. We solve this equation for h. The required height of the dike is then h-h_{bf}.

For coastal flooding, we estimated the km length and required crest height of dikes based on the following procedure, which in essence is similar to targeted local dike safety assessments that evaluate fairly uniform stretches of dikes over coast-normal transects. The procedure involves three steps:

- The derivation of coastal segments and corresponding coast-normal transects.
- The construction of bed-level and vegetation cover based on global maps for each transect.
- The derivation of representative hydrodynamic conditions and wave attenuation under these conditions, resulting in total sea-water level (extreme tide and storm surge and significant wave height and peak wave period) at the foot of the coastal defense, based on which a required dike height is calculated.

The length and position of the coastline is derived from the OpenStreetMap (OSM 2015) coastline, which is approximately located at the mean sea level contour. The coastline was moved 100 m inland to remove small features and derive a smoothed coastline at a likely position to efficiently establish a dike system. To find representative foreshore characteristics for the coastline, the world was divided in 1′ × 1′ (ca. 2 km × 2 km at the equator) grid cells. For every cell containing a coastline segment, its coastline length and a transect perpendicular to the coast were derived at the center of the segment, resulting in 495,361 transects that are on average 1.1 km apart. The analysis was limited to latitudes between 60° north and south for reasons of data availability and socioeconomic relevance. To test the sensitivity of the model to the transect spacing, transects based on a higher-resolution 30″x 30″ grid were derived for small coastal sections. Bootstrapping from these densely spaced transects revealed that transect distances up to 2 km give very similar results, indicating that a granularity of ~1.1 km is high enough.

Figure A6 | **Schematic Overview of Characteristics Used to Define the Foreshore in Each Transect**

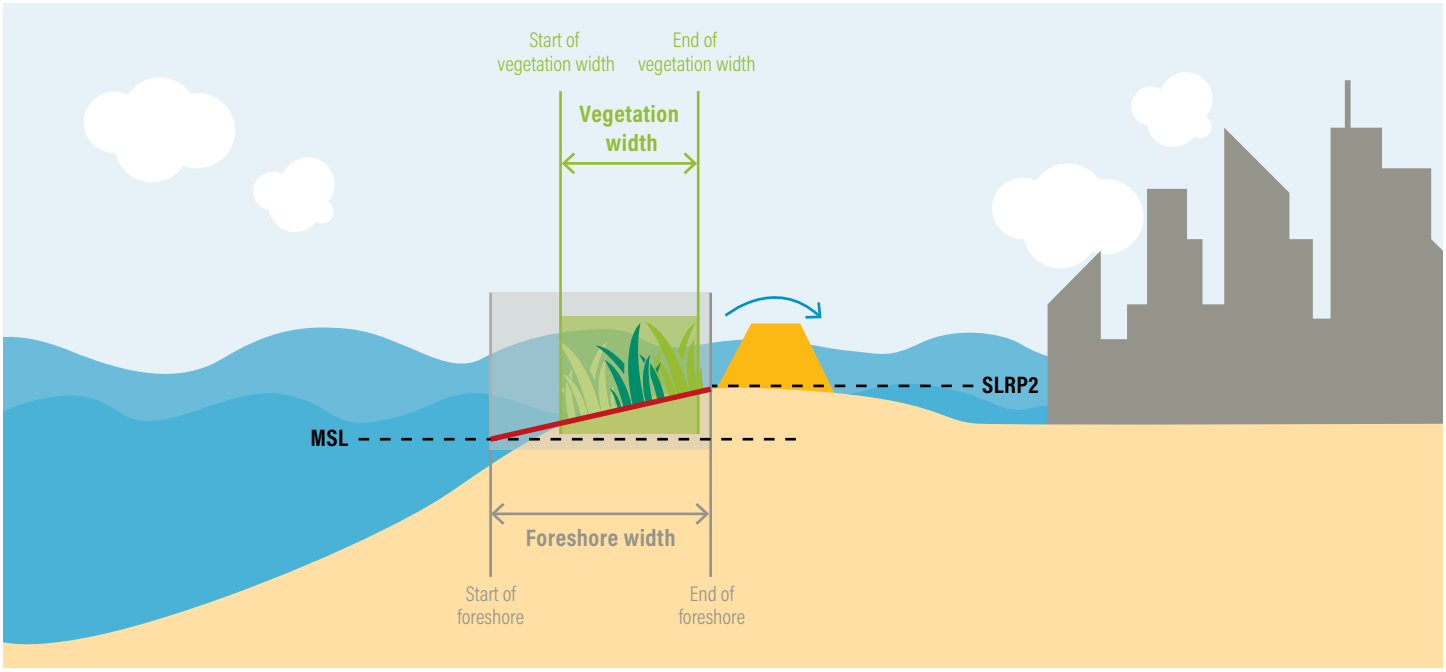

Source: Authors.

For each transect, the foreshore width and slope and the vegetation width and type within the foreshore are derived along a coast-normal transect (see Figure A6). Because the position of the coastline is not accurate everywhere, all transects stretch 4 km seaward and 4 km inland to fully capture the characteristics of most foreshores. The main source of bed-level data is the newly created Earth observation–based high-resolution intertidal elevation map (Foreshore Assessment using Space Technology [FAST] intertidal elevation product; 20 m horizontal resolution, typically 30–50 cm vertical accuracy) (Calero et al. 2017), which fills the critical gap between bathymetry data (General Bathymetric Chart of the Oceans [GEBCO]; 30 arc seconds horizontally, tens of meters vertically) and topography data (MERIT; 3 arc seconds, 2 m vertically). The intertidal data have the highest horizontal and vertical resolution in the intertidal zone but lack accuracy in some environments where tidal range, image availability, or presence of tidal gauges are limited (e.g., the Mediterranean and Black Seas). Therefore, the intertidal data were classified as invalid in case (1) MERIT-GEBCO bed level is above the governing surge level and the intertidal bed level is below the MERIT-GEBCO bed level or (2) the range in bed levels from the intertidal data is smaller than a minimum threshold, indicating noise rather than a valid signal. The final bed level was constructed using intertidal data where sufficient valid data points were available complemented by the merged GEBCO-MERIT data in areas with small intertidal zones or invalid intertidal data. For this purpose, the GEBCO and MERIT data were merged to create a continuous bathymetry-elevation map by changing the vertical datum of MERIT from EGM96 to mean sea level (MSL) and assuming 0 m + MSL at the OSM coastline.

The FAST coastal vegetation map, based on Landsat-8 and Sentinel-2 satellite images, provides actual vegetation presence with 10 m resolution. Where vegetation is found at the foreshore, the vegetation type is determined by global salt marsh (Mcowen et al. 2017) and mangrove (Giri et al. 2011) maps, complemented with Corine Land Cover (CLC) (Europe only) and GlobCover v2.2 maps where the former lack coverage. The salt marsh and mangrove maps are composed of various local datasets of varying quality and have good coverage in Europe and the United States but lack cover in some remote or less-developed regions and countries that did not contribute data, such as northern Canada, northern Africa, southern Chile, Korea, Japan, and Russia. The properties of the vegetation relevant for wave attenuation (spatial density, height, diameter, and drag coefficient) have been determined in the FAST project based on field measurements and literature. Unsurprisingly, these differ considerably between salt marshes and mangroves, but there is no actual vegetation density, such as seasonal variation or difference between temperate and warm climate marshes; the used values are a conservative evaluation of winter properties in order not to overestimate wave attenuation.

The design water levels—tide and storm surge combined—were derived from the GTSR dataset (Muis et al. 2016), while the corresponding wave conditions have been derived from the ERA-Interim reanalysis (Dee et al. 2011). These are offshore significant wave heights and peak periods for a range of return periods (1–1,000 years), transformed to a nearshore wave height that is limited by depth-induced breaking. Consequently, these wave heights for low return periods are typically higher than occur in reality, but the comparison of dike heights between with and without vegetation cover remains informative. A global nearshore wave climate dataset is not available; correctly deriving such a dataset would require an enormous computational effort involving wave models like Simulating Waves Nearshore (SWAN) or Wave Modelling (WAM).

To determine the wave attenuation over a foreshore and the resulting significant wave height relevant for the flood defense on a transect, we used a lookup table with numerical modeling results for 31,824 combinations of foreshore slopes, vegetation covers, and hydrodynamic conditions. The values for these input conditions are based on the expected range of conditions; that is, the distribution functions of these parameters globally. This table contained wave heights modeled by XBeach (a nearshore wave model that accounts for the presence of vegetation; van Rooijen et al. 2016) at regular intervals along a steady slope, both with and without salt marsh or mangrove vegetation. Whereas a steady slope may appear overly simple for foreshore areas with small topographical features like ridges and gullies, the computed wave attenuation is typically comparable to the results of detailed simulations (van Zelst 2018). This method also has much lower computation cost and avoids a false sense of accuracy that high-resolution simulations based on global data may give. Every transect was evaluated coast-normal; that is, the incoming wave runs perpendicular to the coast. This simplification is made because the incoming wave direction is not known; the coast-normal situation is the most conservative because the width of the foreshore is shortest.

The empirical EuroTop formulations (Pullen et al. 2007) give the required dike height with respect to the surge level for a standard 1:3 dike profile without berms and an allowed overtopping discharge of 1 $l/m^2/s$, which is representative for simple, low-cost dikes but conservative for well-constructed and maintained dikes. The wave attenuation and wave run-up were looked up from the condition closest to the foreshore characteristics encountered in the transect under consideration to establish required dike crest height—and possible reduction of this height by vegetation.

In order to determine where dikes are required in terms of occurring flood hazard, the most severe flooding scenario (i.e., 1,000-year return period RCP8.5) was overlaid with the transects. In total, for about 21 percent of all segments a flood may occur and thus a dike is taken into account in the cost-benefit analysis.

ENDNOTES

1. All values in the official International Institute for Applied Systems Analysis (IIASA) databases are expressed in 2005 US$ PPP for consistency across studies.
2. The users may overwrite the FLOPROS flood protection level with any value between 2 and 1,000 (in return period).
3. One alteration was made to the FLOPROS data due to an underestimation: riverine and coastal flood protection values for states within the Netherlands were set to 1,000.
4. The flood protection, in return years, is first converted into a probability before being added to the calculation (i.e., 1/flood protection).
5. Tool label: Implementation Range.
6. Tool label: Infrastructure Lifetime.
7. Tool label: Existing Protection Level (Return Period). See Section 6 to learn about default values.
8. Tool label: Design Protection Level (Return Period).
9. Tool label: Target Year for the Design Protection Level.
10. Interpolation is calculated using the Scipy module's interp1d function in Python (SciPy community, 2019).
11. Tool label: Benefits Start Year.
12. Tool label: Unit Cost ($million/m/km).
13. Tool label: Operation & Maintenance Cost (%).
14. Tool label: Annual Discount Rate (%).

REFERENCES

Aerts, J.C.J.H., W.J.W. Botzen, H. de Moel, and M. Bowman. 2013. "Cost Estimates for Flood Resilience and Protection Strategies in New York City." *Annals of the New York Academy of Sciences* 1294: 1–104. https://doi.org/10.1111/nyas.12200.

Angel, S., A. Chabaeva, L. Gitlin, A. Kraley, J. Parent, and M. Perlin. 2005. "The Dynamics of Global Urban Expansion." Working Paper no. 35563. Washington, DC: World Bank.

Angel, S., J. Parent, D.L. Civco, and A.M. Blei. 2012. Atlas of Urban Expansion [dataset]. Cambridge, MA: Lincoln Institute of Land Policy.

Balk, D.L., U. Deichmann, G. Yetman, F. Pozzi, S.I. Hay, and A. Nelson. 2006. "Determining Global Population Distribution: Methods, Applications and Data." *Advances in Parasitology* 62: 119–56. https://doi.org/10.1016/S0065-308X(05)62004-0.

Bos, A.J. 2008. *Optimal Safety Level for the New Orleans East Polder: A Preliminary Risk Analysis*. Vrei Universiteit Amsterdam.

Bouwman, A.F., T. Kram, T., and K. Klein Goldewijk, eds. 2006. *Integrated Modelling of Global Environmental Change: An Overview of IMAGE 2.4*. Bilthoven: Netherlands Environmental Assessment Agency.

BPIE (Buildings Performance Institute Europe). 2011. *Europe's Buildings under the Microscope: A Country by Country Review of the Energy Performance of Buildings*. Brussels: BPIE.

Bright, E.A., P.R. Coleman, A.N. Rose, and M.L. Urban. 2011. LandScan 2010 High Resolution Global Population Data Set [dataset]. Oak Ridge, TN: Oak Ridge National Laboratory.

Bright, E.A., P.R. Coleman, and A.N. Rose. 2013. LandScan Global Population Database 2013 [dataset]. Oak Ridge, TN: Oak Ridge National Laboratory.

Brown, S., and R.J. Nicholls. 2015. "Subsidence and Human Influences in Mega Deltas: The Case of the Ganges-Brahmaputra-Meghna." *Science of the Total Environment* 527–28: 362–74. https://doi.org/10.1016/j.scitotenv.2015.04.124.

Calero, J.S., G. Hendriksen, J. Dijkstra, A.C. van der Lelij, M. de Vries, R. Ekkelenkamp, and E.P. Morris. 2017. "Fast MI-SAFE Platform: Foreshore Assessment Using Space Technology." Paper presented at Conference on Big Data from Space, Toulouse, France, November 27–30.

Carrère, L., and F. Lyard. 2003. "Modeling the Barotropic Response of the Global Ocean to Atmospheric Wind and Pressure Forcing: Comparisons with Observations." *Geophysical Research Letters* 30. https://doi.org/10.1029/2002GL016473

CIESIN (Center for International Earth Science Information Network), IFPRI (International Food Policy Research Institute), World Bank, and CIAT (Centro Internacional de Agricultura Tropical). 2011. Global Rural-Urban Mapping Project, Version 1 (GRUMPv1): Urban Extents Grid. https://doi.org/10.7927/H4GH9FVG.

Compass International Consultants. 2009. *The 2009 Global Construction Cost and Reference Yearbook*.

de Graaf, I.E.M., R.L.P.H. van Beek, T. Gleeson, N. Moosdorf, O. Schmitz, E.H. Sutanudjaja, and M.F.P. Bierkens. 2017. "A Global-Scale Two-Layer Transient Groundwater Model: Development and Application to Groundwater Depletion." *Advances in Water Resources* 102: 53–67. https://doi.org/10.1016/j.advwatres.2017.01.011.

De Grave, P., and G. Baarse. 2011. *Kosten van maatregelen: Informatie ten behoeve van het project Waterveiligheid 21e eeuw*. Delft, the Netherlands: Deltares.

Dee, D.P., S.M. Uppala, A.J. Simmons, P. Berrisford, P. Poli, S. Kobayashi, U. Andrae, et al. 2011. "The ERA-Interim Reanalysis: Configuration and Performance of the Data Assimilation System." *Quarterly Journal of the Royal Meteorological Society* 137: 553–97. https://doi.org/10.1002/qj.828.

Defourny, P. 2016. ESA Land Cover Climate Change Initiative (Land_Cover_cci): Water Bodies Map, v4.0 [dataset]. Chilton, UK: Centre for Environmental Data Analysis.

EEA (European Environment Agency). 2016. Corine Land Cover 2012 seamless 100m raster database, data file. Release February 19.

Erkens, G., T. Bucx, R. Dam, G. de Lange, and J. Lambert. 2015. "Sinking Coastal Cities." In *Proceedings of the International Association of Hydrological Sciences,* 189–98. Presented at Prevention and Mitigation of Natural and Anthropogenic Hazards Due to Land Subsidence, Ninth International Symposium on Land Subsidence (NISOLS), Nagoya, Japan, November 19. https://doi.org/10.5194/piahs-372-189-2015.

Erkens, G., and E.H. Sutanudjaja. 2015. "Towards a Global Land Subsidence Map." *Proceedings of the International Association of Hydrological Sciences* 372: 83–87. https://doi.org/10.5194/piahs-372-83-2015.

Friedl, M.A., D.K. McIver, J.C.F. Hodges, X.Y. Zhang, D. Muchoney, A.H. Strahler, C.E. Woodcock, et al. 2002. "Global Land Cover Mapping from MODIS: Algorithms and Early Results." In "The Moderate Resolution Imaging Spectroradiometer (MODIS): A New Generation of Land Surface Monitoring," special issue of *Remote Sensing of Environment* 83: 287–302. https://doi.org/10.1016/S0034-4257(02)00078-0.

GADM (Global Administrative Areas). 2012. The database of Global Administrative Areas.

Galloway, D.L., G. Erkens, E.L. Kuniansky, and J.C. Rowland. 2016. "Preface: Land Subsidence Processes." *Hydrogeology Journal* 24: 547–50. https://doi.org/10.1007/s10040-016-1386-y.

Gennaioli, N., R. La Porta, F. Lopez-de-Silanes, and A. Shleifer. 2013. "Human Capital and Regional Development." *Quarterly Journal of Economics* 128: 105–64. https://doi.org/10.1093/qje/qjs050.

Gesch, D.B., K.L. Verdin, and S.K. Greenlee. 1999. "New Land Surface Digital Elevation Model Covers the Earth." *Eos, Transactions American Geophysical Union* 80: 69–70. https://doi.org/10.1029/99EO00050.

Giri, C., E. Ochieng, L.L. Tieszen, Z. Zhu, A. Singh, T. Loveland, J. Masek, and N. Duke. 2011. "Status and Distribution of Mangrove Forests of the World Using Earth Observation Satellite Data." *Global Ecology and Biogeography* 20: 154–59. https://doi.org/10.1111/j.1466-8238.2010.00584.x.

Hallegatte, S., C. Green, R.J. Nicholls, and J. Corfee-Morlot. 2013. "Future Flood Losses in Major Coastal Cities." *Nature Climate Change* 3: 802–6. https://doi.org/10.1038/nclimate1979.

Harbaugh, A.W., E.R. Banta, M.C. Hill, and M.G. McDonald. 2000. *MODFLOW-2000: The U.S. Geological Survey Modular Ground-Water Model—User Guide to Modularization Concepts and the Ground-Water Flow Process*. USGS Numbered Series No. 2000–92. Open-File Report. Washington, DC: U.S. Geological Survey.

Hartmann, J., and N. Moosdorf. 2012. "The New Global Lithological Map Database GLiM: A Representation of Rock Properties at the Earth Surface." *Geochemistry, Geophysics, Geosystems* 13. https://doi.org/10.1029/2012GC004370.

Hempel, S., K. Frieler, L. Warszawski, J. Schewe, and F. Piontek. 2013. "A Trend-Preserving Bias Correction: The ISI-MIP Approach." *Earth System Dynamics* 4 (2): 219–36. doi:https://doi.org/10.5194/esd-4-219-2013.

Hinkel, J., D. Lincke, A.T. Vafeidis, M. Perrette, R.J. Nicholls, R.S.J. Tol, B. Marzeion, et al. 2014. "Coastal Flood Damage and Adaptation Costs under 21st Century Sea-Level Rise." *Proceedings of the National Academy of Sciences* 111: 3292–97. https://doi.org/10.1073/pnas.1222469111.

Huizinga, J., H. de Moel, and W. Szewczyk. 2017. "Global Flood Depth-Damage Functions." Publications Office of the European Union 114.

IIASA (International Institute for Applied Systems Analysis). 2013. SSP database [dataset].

IUCN (International Union for Conservation of Nature) and UNEP-WCMC (UNEP World Conservation Monitoring Centre). 2009. The World Database on Protected Areas (WDPA) [dataset].

Jarvis, A., H.I. Reuter, A. Nelson, and E. Guevara. 2006. Hole-Filled SRTM for the Globe Version 3, from the CGIAR-CSI SRTM 90 m database [dataset]. CGIAR-Consortium for Spatial Information.

Jevrejeva, S., A. Grinsted, and J.C. Moore. 2014. "Upper Limit for Sea Level Projections by 2100." *Environmental Research Letters* 9: 104008. https://doi.org/10.1088/1748-9326/9/10/104008.

Jiang, L., and B.C. O'Neill. 2017. "Global Urbanization Projections for the Shared Socioeconomic Pathways." *Global Environmental Change* 42: 193–99. https://doi.org/10.1016/j.gloenvcha.2015.03.008.

Johnson, F., S. Westra, A. Sharma, and A.J. Pitman. 2011. "An Assessment of GCM Skill in Simulating Persistence across Multiple Time Scales." *Journal of Climate* 24: 3609–23. https://doi.org/10.1175/2011JCLI3732.1.

Jongman, B., P.J. Ward, and J.C.J.H. Aerts. 2012. "Global Exposure to River and Coastal Flooding: Long Term Trends and Changes." *Global Environmental Change* 22: 823–35. https://doi.org/10.1016/j.gloenvcha.2012.07.004.

Jongman, B., H.C. Winsemius, J.C.J.H. Aerts, E.C. de Perez, M.K. van Aalst, W. Kron, and P.J. Ward. 2015. "Declining Vulnerability to River Floods and the Global Benefits of Adaptation." *Proceedings of the National Academy of Sciences* 112: E2271–80. https://doi.org/10.1073/pnas.1414439112.

Jonkman, S.N., M.M. Hillen, R.J. Nicholls, W. Kanning, and M. van Ledden. 2013. "Costs of Adapting Coastal Defences to Sea-Level Rise: New Estimates and Their Implications." *Journal of Coastal Research* 1212–26. https://doi.org/10.2112/JCOASTRES-D-12-00230.1.

Klein Goldewijk, K., A. Beusen, and P. Janssen. 2010. "Long-Term Dynamic Modeling of Global Population and Built-Up Area in a Spatially Explicit Way: HYDE 3.1." *Holocene* 20: 565–73. https://doi.org/10.1177/0959683609356587.

Klein Goldewijk, K., A. Beusen, J. Doelman, and E. Stehfest. 2017. "Anthropogenic Land Use Estimates for the Holocene: HYDE 3.2." *Earth System Science Data* 9: 927–53. https://doi.org/10.5194/essd-9-927-2017.

Kooi, H., M. Bakr, G. de Lange, E. den Hann, and G. Erkens. 2018. *A User Guide to SUB-CR: A Modflow Land Subsidence and Aquifer System Compaction Package That Includes Creep*. Delft, the Netherlands: Deltares.

Lehner, B., K. Verdin, and A. Jarvis. 2008. "New Global Hydrography Derived from Spaceborne Elevation Data." *Eos, Transactions American Geophysical Union* 89: 2. https://doi.org/10.1029/2008EO100001.

Lenk, S., D. Rybski, O. Heidrich, R.J. Dawson, and J.P. Kropp. 2017. "Costs of Sea Dikes: Regressions and Uncertainty Estimates." *Natural Hazards and Earth System Sciences* 17: 765–79. https://doi.org/10.5194/nhess-17-765-2017.

Loonen, W., E. Koomen, and M. Kuijpers-Linde. 2009. "Calibrating and Validating the Land Use Scanner Algorithms." PBL Netherlands Environmental Assessment Agency 4.

Mcowen, C.J., L.V. Weatherdon, J.-W.V., Bochove, E. Sullivan, S. Blyth, C. Zockler, D. Stanwell-Smith, et al. 2017. "A Global Map of Saltmarshes." *Biodiversity Data Journal* e11764. https://doi.org/10.3897/BDJ.5.e11764.

Meyer, V., D. Haase, and S. Scheuer. 2009. "Flood Risk Assessment in European River Basins: Concept, Methods, and Challenges Exemplified at the Mulde River." *Integrated Environmental Assessment and Management* 5: 17–26. https://doi.org/10.1897/IEAM_2008-031.1.

Muis, S., M. Verlaan, H.C. Winsemius, J.C.J.H. Aerts, and P.J. Ward. 2016. "A Global Reanalysis of Storm Surges and Extreme Sea Levels." *Nature Communications* 7: 11969. https://doi.org/10.1038/ncomms11969.

Muis, S., M. Verlaan, R.J. Nicholls, S. Brown, J. Hinkel, D. Lincke, A.T. Vafeidis, et al. 2017. "A Comparison of Two Global Datasets of Extreme Sea Levels and Resulting Flood Exposure." *Earth's Future* 5: 379–92. https://doi.org/10.1002/2016EF000430.

Nobre, A.D., L.A. Cuartas, M. Hodnett, C.D. Rennó, G. Rodrigues, A. Silveira, M. Waterloo, and S. Saleska. 2011. "Height above the Nearest Drainage: A Hydrologically Relevant New Terrain Model." *Journal of Hydrolology* 404: 13–29. https://doi.org/10.1016/j.jhydrol.2011.03.051.

OSM (OpenStreetMap). 2015. OpenStreetMap. https://www.openstreetmap.org/.

PBL (Netherlands Environmental Assessment Agency). 2009. Global Roads Inventory Project (GRIP) dataset v1. The Hague: PBL.

PBL. 2018. "Towards an Urban Preview: Modelling Future Urban Growth with 2UP." No. 3255. The Hague: PBL.

Pekel, J.-F., A. Cottam, N. Gorelick, A.S. Belward. 2016. "High-Resolution Mapping of Global Surface Water and Its Long-Term Changes." *Nature* 540: 418–22. https://doi.org/10.1038/nature20584.

Pullen, T., N.W.H. Allsop, T. Bruce, A. Kortenhaus, H. Schüttrumpf, and J.W. Van der Meer. 2007. *EurOtop, European Overtopping Manual: Wave Overtopping of Sea Defences and Related Structures: Assessment Manual*. Environment Agency (U.K.), Expertise Netwerk Waterkeren (Netherlands), and Kuratorium für Forschung im Küsteningenieurwesen (Germany).

Riley, S., S. Degloria, and S.D. Elliot. 1999. "A Terrain Ruggedness Index That Quantifies Topographic Heterogeneity." *Intermountain Journal of Sciences* 5: 23–27.

Schellekens, J. 2014. *wflow* documentation. Delft, the Netherlands: Deltares.

SciPy community. 2019. SciPy v1.2.1 Reference Guide. scipy.interpolate.interp1d.

Scussolini, P., J.C.J.H. Aerts, B. Jongman, L.M. Bouwer, H.C. Winsemius, H. de Moel, and P.J. Ward. 2016. "FLOPROS: An Evolving Global Database of Flood Protection Standards." *Natural Hazards and Earth System Sciences* 16: 1049–61. https://doi.org/10.5194/nhess-16-1049-2016.

Sutanudjaja, E.H., R. van Beek, N. Wanders, Y. Wada, J.H.C. Bosmans, N. Drost, R.J. van der Ent, et al. 2018. "PCR-GLOBWB 2: A 5 Arcmin Global Hydrological and Water Resources Model." *Geoscientific Model Development* 11: 2429–53. https://doi.org/10.5194/gmd-11-2429-2018.

Syvitski, J.P.M., A.J. Kettner, I. Overeem, E.W.H. Hutton, M.T. Hannon, G.R. Brakenridge, J. Day, et al. 2009. "Sinking Deltas Due to Human Activities." *Nature Geoscience* 2: 681–86. https://doi.org/10.1038/ngeo629.

UNISDR (United Nations International Strategy for Disaster Reduction). 2015. *The Human Cost of Weather Related Disasters, 1995–2015*. https://doi.org/10.13140/RG.2.2.17677.33769.

USGS (U.S. Geological Survey). 1996. Global Digital Elevation Model (GTOPO30) [dataset]. EROS Data Center.

Vafeidis, A.T., M. Schuerch, C. Wolff, T. Spencer, J.L. Merkens, J. Hinkel, D. Lincke, et al. 2018. "Water-Level Attenuation in Broad-Scale Assessments of Exposure to Coastal Flooding: A Sensitivity Analysis." *Natural Hazards and Earth System Sciences Discussion Papers* 1–19. https://doi.org/10.5194/nhess-2018-359.

Van Beek, L.P.H., Y. Wada, and M.F.P. Bierkens. 2011. "Global Monthly Water Stress: 1. Water Balance and Water Availability." *Water Resources Research* 47. https://doi.org/10.1029/2010WR009791.

van Rooijen, A.A., R.T. McCall, J.S.M. van Thiel de Vries, A.R. van Dongeren, A.J.H.M. Reniers, and J.A. Roelvink. 2016. "Modeling the Effect of Wave-Vegetation Interaction on Wave Setup." *Journal of Geophysical Research: Oceans* 121: 4341–59. https://doi.org/10.1002/2015JC011392.

van Vuuren, D.P., J. Edmonds, M. Kainuma, K. Riahi, A. Thomson, K. Hibbard, G.C. Hurtt, et al. 2011. "The Representative Concentration Pathways: An Overview." *Climate Change* 109: 5. https://doi.org/10.1007/s10584-011-0148-z.

van Vuuren, D.P., E. Kriegler, B.C. O'Neill, K.L. Ebi, K. Riahi, T.R. Carter, J. Edmonds, et al. 2014. "A New Scenario Framework for Climate Change Research: Scenario Matrix Architecture." *Climate Change* 122: 373–86. https://doi.org/10.1007/s10584-013-0906-1.

van Wesenbeeck, B.K., J. Dijkstra, H.C. Winsemius, M. de Vires, P. Herman, B. Evans, E., Morris, et al. n.d. "The Role of Coastal Vegetation in Global Risk Reduction."

van Zelst, V. 2018. "Global Flood Hazard Reduction by Foreshore Vegetation." Master's thesis, Delft University of Technology.

Verdin, K.L., and S.K. Greenlee. 1996. "Development of Continental Scale DEMs and Extraction of Hydrographic Features." Paper presented at National Center for Geographic Information and Analysis (NCGIA) International Conference/Workshop on Integrating GIS and Environmental Modeling, Santa Fe, NM.

Vitousek, S., P.L. Barnard, C.H. Fletcher, N. Frazer, L. Erikson, and C.D. Storlazzi. 2017. "Doubling of Coastal Flooding Frequency within Decades Due to Sea-Level Rise." *Scientific Reports* 7: 1399. https://doi.org/10.1038/s41598-017-01362-7.

Ward, M.D., B.D. Greenhill, and K.M. Bakke. 2010. "The Perils of Policy by P-Value: Predicting Civil Conflicts." *Journal of Peace Research*. 47: 363–75. https://doi.org/10.1177/0022343309356491.

Ward, P.J., B. Jongman, J.C.J.H. Aerts, P.D. Bates, W.J.W. Botzen, A. Díaz Loaiza, S. Hallegatte, et al. 2017. "A Global Framework for Future Costs and Benefits of River-Flood Protection in Urban Areas." *Nature Climate Change* 7: 642–46. https://doi.org/10.1038/nclimate3350.

Ward, P.J., B. Jongman, M. Kummu, M.D. Dettinger, F.C.S. Weiland, and H.C. Winsemius. 2014. "Strong Influence of El Niño Southern Oscillation on Flood Risk around the World." *Proceedings of the National Academy of Sciences* 111: 15659–64. https://doi.org/10.1073/pnas.1409822111.

Ward, P.J., B. Jongman, F.S. Weiland, A. Bouwman, R. van Beek, M.F.P. Bierkens, W. Ligtvoet, and H.C. Winsemius. 2013. "Assessing Flood Risk at the Global Scale: Model Setup, Results, and Sensitivity." *Environmental Research Letters* 8: 044019. https://doi.org/10.1088/1748-9326/8/4/044019.

Weedon, G.P., S. Gomes, P. Viterbo, W.J. Shuttleworth, E. Blyth, H. Österle, J.C. Adam, et al. 2011. "Creation of the WATCH Forcing Data and Its Use to Assess Global and Regional Reference Crop Evaporation over Land during the Twentieth Century." *Journal of Hydrometeorology* 12: 823–48. https://doi.org/10.1175/2011JHM1369.1.

Winsemius, H.C., J.C.J.H. Aerts, L.P.H. van Beek, M.F.P. Bierkens, A. Bouwman, B. Jongman, J.C.J. Kwadijk, et al. 2016. "Global Drivers of Future River Flood Risk." *Nature Climate Change* 6: 381–85. https://doi.org/10.1038/nclimate2893.

Winsemius, H.C., L.P.H. van Beek, B. Jongman, P.J. Ward, and A. Bouwman. 2013. "A Framework for Global River Flood Risk Assessments." *Hydrology and Earth System Sciences* 17: 1871–92. https://doi.org/10.5194/hess-17-1871-2013.

Woodruff, J.D., J.L. Irish, and S.J. Camargo. 2013. "Coastal Flooding by Tropical Cyclones and Sea-Level Rise." *Nature* 504: 44–52. https://doi.org/10.1038/nature12855.

Yamazaki, D., D. Ikeshima, R. Tawatari, T. Yamaguchi, F. O'Loughlin, J.C. Neal, C.C. Sampson, et al. 2017. "A High-Accuracy Map of Global Terrain Elevations." *Geophysical Research Letters* 44: 5844–53. https://doi.org/10.1002/2017GL072874.

ABOUT THE AUTHORS

Philip J. Ward is Professor of Global Water Risk Dynamics and Head of the Global Water and Climate Risk section of the Vrije Universiteit Amsterdam's Institute for Environmental Studies.

Contact: philip.ward@vu.nl

Hessel C. Winsemius is an Associate Professor in the Water Management Department at Delft University of Technology and a Senior Researcher/Advisor at Deltares.

Contact: h.c.winsemius@tudelft.nl

Samantha Kuzma is an Associate at the World Resources Institute.

Contact: samantha.kuzma@gmail.com

Marc F.P. Bierkens is the Chair of Earth Surface Hydrology in the Department of Physical Geography at Utrecht University.

Arno Bouwman is a researcher at PBL (Netherlands Environmental Assessment Agency).

Hans de Moel is an Assistant Professor at Vrije Universiteit Amsterdam's Institute for Environmental Studies.

Andrés Díaz Loaiza is a postdoctoral researcher at Vrije Universiteit Amsterdam's Institute for Environmental Studies.

Dirk Eilander is a PhD candidate at Vrije Universiteit Amsterdam's Institute for Environmental Studies and a researcher at Deltares in Delft, the Netherlands.

Johanna Englhardt is a PhD candidate at Vrije Universiteit Amsterdam's Institute for Environmental Studies.

Gilles Erkens is a researcher at Deltares in Delft, the Netherlands.

Eskedar Tafete Gebremedhin is a researcher and Junior Advisor at Deltares in Delft, the Netherlands.

Charles Iceland is a Director at the World Resources Institute.

Henk Kooi is a researcher at Deltares in Delft, the Netherlands.

Willem Ligtvoet is a researcher at PBL (Netherlands Environmental Assessment Agency).

Sanne Muis is an Assistant Professor at Vrije Universiteit Amsterdam's Institute for Environmental Studies and a researcher at Deltares in Delft, the Netherlands.

Paolo Scussolini is a postdoctoral researcher at Vrije Universiteit Amsterdam's Institute for Environmental Studies.

Edwin H. Sutanudjaja is the core developer of PCR-GLOBWB 2 in the Department of Physical Geography at Utrecht University.

Rens van Beek is an Assistant Professor in the Department of Physical Geography at Utrecht University.

Bas van Bemmel is a researcher at PBL (Netherlands Environmental Assessment Agency).

Jolien van Huijstee is a researcher at PBL (Netherlands Environmental Assessment Agency).

Frank van Rijn is a researcher at PBL (Netherlands Environmental Assessment Agency).

Bregje van Wesenbeeck is a Senior Advisor at Deltares in Delft, the Netherlands.

Deepak Vatvani is a Senior Advisor at Deltares in Delft, the Netherlands.

Martin Verlaan is a Senior Advisor at Deltares in Delft, the Netherlands.

Timothy Tiggeloven is a PhD candidate at Vrije Universiteit Amsterdam's Institute for Environmental Studies.

Tianyi Luo is a Senior Manager at World Resources Institute.

Contact: Tianyi.Luo@wri.org

ACKNOWLEDGMENTS

We are pleased to acknowledge our institutional strategic partners, who provide core funding to WRI: Netherlands Ministry of Foreign Affairs, Royal Danish Ministry of Foreign Affairs, and Swedish International Development Cooperation Agency.

This publication was made possible thanks to the support of the Netherlands Ministry of Infrastructure and Water Management, the World Bank, the Global Facility for Disaster Reduction and Recovery, and Skoll Global Threats Fund. This study's calculations were computed on the Dutch national supercomputer Cartesius with the support of SURFsara. Philip Ward and VU Amsterdam also received funding from the Netherlands Organisation for Scientific Research (NWO) in the form of a VIDI grant (grant no. 016.161.324)

The authors would like to thank the following people for providing invaluable insight and assistance in the development of this paper: Betsy Otto (WRI), Leah Schleifer (WRI), Emilia Suarez (WRI), and Eliza Swedenborg (WRI); as well as our internal reviewers Lauretta Burke, Helen Ding, and Rutger Hofste; and external reviewers Doug Bausch (Pacific Disaster Center), Yohannes Kesete (World Bank), and Gillian Mollod (MSCI).

The authors would also like to thank our research partners at Deltares, VU-IVM, PBL, and Utrecht University, as well as Vizzuality, Romain Warnault, Carni Klirs, and Billie Kanfer for their extensive guidance and feedback during the design and development of this study.

Opinions or points of view expressed in this report are those of the authors and do not necessarily reflect the position of the reviewers, research partners, or the organizations they represent.

ABOUT WRI

World Resources Institute is a global research organization that turns big ideas into action at the nexus of environment, economic opportunity, and human well-being.

Our Challenge

Natural resources are at the foundation of economic opportunity and human well-being. But today, we are depleting Earth's resources at rates that are not sustainable, endangering economies and people's lives. People depend on clean water, fertile land, healthy forests, and a stable climate. Livable cities and clean energy are essential for a sustainable planet. We must address these urgent, global challenges this decade.

Our Vision

We envision an equitable and prosperous planet driven by the wise management of natural resources. We aspire to create a world where the actions of government, business, and communities combine to eliminate poverty and sustain the natural environment for all people.

Our Approach

COUNT IT

We start with data. We conduct independent research and draw on the latest technology to develop new insights and recommendations. Our rigorous analysis identifies risks, unveils opportunities, and informs smart strategies. We focus our efforts on influential and emerging economies where the future of sustainability will be determined.

CHANGE IT

We use our research to influence government policies, business strategies, and civil society action. We test projects with communities, companies, and government agencies to build a strong evidence base. Then, we work with partners to deliver change on the ground that alleviates poverty and strengthens society. We hold ourselves accountable to ensure our outcomes will be bold and enduring.

SCALE IT

We don't think small. Once tested, we work with partners to adopt and expand our efforts regionally and globally. We engage with decision-makers to carry out our ideas and elevate our impact. We measure success through government and business actions that improve people's lives and sustain a healthy environment.